# Retinoic acid coordinates the orderly construction of the mammalian body in the anterior-to-posterior sequence

Anita Banerjee[1,#], Sameera Krishna Yallapragada[1,#], Gabriel Torregrosa-Cortés[2], Bhakti J Vyas[3], Ramkumar Sambasivan[1,*]

[1] *Indian Institute of Science Education and Research (IISER) Tirupati, Srinivasapuram, Panguru, Yerpedu mandal, Tirupati 517619, Andhra Pradesh, India*

[2] *EMBL Barcelona, Dr. Aiguader, 88, PRBB Building, 08003 Barcelona, Spain*

[3] *Institute for Stem Cell Science and Regenerative Medicine, GKVK-post, Bellary Road, Bengaluru 560065, Karnataka, India*

[#] These authors contributed equally to the work

[*] Correspondence to: ramkumars@labs.iisertirupati.ac.in

## Abstract

In vertebrate embryos, anterior structures are formed early during gastrulation, while the posterior body develops subsequently. This temporal anterior-to-posterior developmental sequence is a fundamental aspect of animal development. Recent studies have shown that discrete regulatory modules involving Nodal and Wnt signaling pathways, in conjunction with T-box factors Eomes and Brachyury (Tbxt), underlie the differential specification of anterior and posterior mesoderm. However, the mechanism governing the transition from anterior to posterior mesoderm development remains unclear. Our findings suggest that retinoic acid signaling regulates the anterior-to-posterior developmental transition. Using mouse embryonic stem cell-based gastruloids, we show that the preclusion of retinoic acid signaling drives anterior mesoderm development, whereas the mesoderm specified in the presence of retinoic acid acquires posterior identity. Our observations indicate that retinoic acid signaling modulates the Wnt pathway. We demonstrate that both *Eomes* and *Tbxt* are essential for suppressing the posterior fate. The negative regulation of Wnt signaling by these T-box factors is critical, along with the preclusion of retinoic acid signaling, to ensure orderly anterior-posterior developmental progression. We propose that the preclusion of retinoic acid signaling early during gastrulation is crucial to maintain low Wnt signal levels, thereby driving anterior mesoderm specification. Subsequently, the activation of retinoic acid signaling results in high Wnt conditions, facilitating a switch to posterior mesoderm development.

## Introduction:

The animal body is constructed in a head-to-tail sequence. During embryogenesis, the anterior structures are specified, followed by the progressive formation of the posterior body (Stern et al., 2006). The deep conservation observed across bilateria highlights the fundamental nature of this mode of development. Despite its fundamental nature, the mechanism of anterior-to-posterior (A-P) developmental progression remains poorly understood. Differentiation of the mesoderm germ layer along the anterior-posterior axis offers an excellent model for investigating A-P progression. Recently, there has been renewed efforts to elucidate the network regulating the differential specification of anterior and posterior mesoderm.

Nodal, a TGFβ superfamily member, and Wnt/β-catenin signaling determine the mesodermal fate of pluripotent epiblast cells in mammalian embryos. These signals induce the expression of T-box transcription factors Eomes and Tbxt (Brachyury or T), which regulate the mesodermal gene network (Ramkumar & Anderson, 2011). In mouse embyros, mesoderm emerging from the early primitive streak between embryonic days E6.5 and E7.5 takes anterior identity (Kinder et al., 1999; Lawson et al., 1991). After E7.5, the late primitive streak gives rise to posterior mesoderm. Eomes and Nodal signaling are essential for anterior mesoderm specification (Arnold et al., 2008; Costello et al., 2011; Simon et al., 2017; Van Den Ameele et al., 2012). Conversely, specification of the posterior mesoderm requires the function of Tbxt and Wnt3a (Herrmann, 1991; Martin & Kimelman, 2008a; Nandkishore et al., 2018; Smith et al., 1991; Takada et al., 1994; Yamaguchi, Takada, et al., 1999). Wnt/β-catenin signaling imparts posterior identity via the activation of caudal homeobox factors, specifically Cdx2 (Ikeya & Takada, 2001; Lickert et al., 2000; Pilon et al., 2006, 2007). The Wnt-Cdx axis appears to be a deeply conserved pathway governing embryonic posterior development across bilateria (Martin & Kimelman, 2009).

The transition from early to late streak is marked by a shift from *Wnt3* to *Wnt3a* expression (Yamaguchi, 2001), correlating with decreased *Eomes* and increased *Tbxt* expression in the newly formed mesoderm (Wehmeyer et al., 2025). Although *Eomes* and *Tbxt* are co-expressed in the early streak, Eomes restricts Tbxt function, promoting an anterior trajectory (Schüle et al., 2023). Recent studies have demonstrated that low Wnt signaling, established by the Nodal-Eomes-Wnt3 network, specify the anterior mesoderm, whereas high Wnt signaling, established by the Tbxt-Wnt3a network, specifies the posterior mesoderm (Dias et al., 2025; Wehmeyer et al., 2025). Furthermore, the activation of the positive feedback module of Wnt signaling and Cdx2, a caudal homeobox factor of the parahox cluster, signifies the transition to a posterior developmental programme (Amin et al., 2016; van de Ven et al., 2011; van Rooijen et al., 2012; Young et al., 2009; Young & Deschamps, 2009). These investigations led to a model of regulatory networks governing the differential specification of anterior and posterior mesoderm. However, the

mechanism underlying the transition from the anterior to the posterior program remains elusive.

Retinoic acid (RA) is undetectable in early mouse gastrulae, and its synthesis begins around embryonic day 7.5 (E7.5) with the activation of Aldh1a2 in the differentiating paraxial mesoderm (Ang et al., 1996; Rossant et al., 1991). Notably, maternal RA is degraded in early streak embryos by Cyp26a enzymes to maintain a RA-negative environment (Uehara et al., 2009). Although the posterior mesoderm is specified, *Aldh1a2*$^{-/-}$ mouse embryos display severe reduction in the posterior body elongation (Niederreither et al., 1999). Moreover, it is well established that RA signaling regulates body axis patterning through the regulation of Hox genes (Nolte et al., 2019). While the correlation between the initiation of RA signaling and early-to-late streak transition is evident, the causality has not been investigated. Although the role of RA in axial patterning following the activation of the posterior program has been extensively studied, its potential function in specifying anterior identity or in the A-P developmental transition remains to be elucidated.

Using mouse embryonic stem cell-derived gastruloids and single-cell transcriptomics, we demonstrate that the inhibition of retinoic acid (RA) signaling permits the specification of anterior mesoderm, whereas the presence of RA leads to posterior mesoderm specification. In the absence of RA signaling, Wnt/β-catenin signaling is attenuated. Taken together with the recent findings that a high Wnt signaling threshold accelerates the transition to posterior mesoderm, our study indicates that RA regulates the A-P transition by modulating the Wnt signaling pathway. Furthermore, using genetics, we reveal that *Eomes* is essential for suppressing the Wnt-Cdx2 module to inhibit the posterior fate. Surprisingly, suppression of the posterior fate in the absence of RA also requires *Tbxt* function. In the absence of RA, increased Wnt signaling in *Tbxt* mutants promotes posterior neural fate. Since the activation of Wnt-Cdx2 in the absence of either *Eomes* or *Tbxt* overrides the need for RA signaling for posterior fate specification, we infer that RA functions upstream of the Wnt-Cdx module to regulate the A-P progression. Collectively, our findings suggest that the transition from an RA-negative early streak to an RA-active late-streak stage promotes the orderly A-P developmental transition.

## Results:

### Preclusion of the RA signal specifies anterior mesoderm

Classical gastruloids are characterized by the presence of post-occipital embryonic tissues (Beccari et al., 2018; Turner et al., 2017). Although cardiomyocytes, which originate from the anterior mesoderm, have been successfully derived through the application of exogenous cardiogenic factors (Rossi et al., 2021), the mesoderm generated in these gastruloids predominantly consists of the posterior subtype, with limited specification of the anterior mesoderm (Mayran et al., 2025; Rekaik et al., 2023; Rosen et al., 2022; Suppinger et al., 2023; van den Brink et al., 2020). Hence, we refer to the classical gastruloids as posterior mesoderm (PM) gastruloids here. We modulated the signaling cues in this model to investigate the mechanism underlying the differential specification of anterior and posterior mesoderm.

Wnt/β-catenin, Nodal, and FGF signaling pathways are key regulators of early mesoderm development in the mouse gastrula (Arnold & Robertson, 2009; Ciruna & Rossant, 2001; Ramkumar & Anderson, 2011), and several studies have focused on these pathways. In contrast, the RA signaling pathway has been less extensively studied in this context. Studies have shown that RA is not synthesized in the embryos early on, and maternal RA is excluded during early mouse gastrulation when the anterior mesoderm emerges from the primitive streak (Ang et al., 1996; Rossant et al., 1991; Uehara et al., 2009). RA synthesis begins around embryonic day E7.5, coinciding with the transition to posterior mesoderm formation (Ang et al., 1996; Rossant et al., 1991). Analysis of the single-cell ATLAS of mouse gastrulation (Pijuan-Sala et al., 2019) revealed that *Aldh1a2* RNA, encoding a critical enzyme in RA biosynthesis from Vitamin A, could be barely detected in the primitive streak and nascent mesoderm of early gastrulae, whereas the transcripts of RA-degrading cytochrome oxidase enzyme *Cyp26A1* showed strong expression (Figure S1, A-B). Given the role of RA in posterior patterning (Durston et al., 1989; Kessel & Gruss, 1991; Ruiz I Altaba & Jessell, 1991), we hypothesized that exclusion of RA may be essential for specifying the anterior mesoderm. To test this hypothesis, we generated gastruloids in the absence of vitamin A, the precursor of RA (Figure 1A). Mouse embryonic stem cells (ESCs) were cultured in N2B27 medium, using a version of B27 devoid of vitamin A. Unlike PM gastruloids, these gastruloids showed limited elongation at 120 hours (h) (Figure 1, B-C). They exhibited robust expression of Isl1, a cardiopharyngeal mesoderm marker which is a subset of the anterior mesoderm (Figure 1B). Notably, the posterior pole, characterized by polarized Tbxt and Cdx2 expression, was absent. Tbxt was expressed in a nonpolar manner, and Cdx2 expression was greatly reduced and overlapped with that of Tbxt (Figure 1B, D). These observations suggest that inducing Wnt signaling in the absence of the RA signal specifies anterior mesoderm, and suppresses Cdx2 expression and posterior pole formation. Notably, the minus

vitamin A gastruloids differentiated to generate beating cardiac organoids when the culture was continued beyond 144h in the presence of cardiogenic factors, FGF10 and IGF1 (Figure 1E). The efficient cardiac differentiation underscored the anterior identity of the mesoderm formed in these gastruloids. As these gastruloids form the anterior mesoderm, we designated them anterior mesoderm (AM) gastruloids.

Analysis of the RA signal reporter RARE-d2eGFP showed that RA signaling was undetectable in the minus vitamin A / AM gastruloids but was active in the posterior mesoderm (PM) gastruloids (Figure 1F). Furthermore, the inhibition of RA signaling through the use of an RA receptor antagonist AGN193109 during gastruloid generation replicated the AM-gastruloid phenotype (Figure 1, F-G). On the other hand, when RA is added exogenously, the 'minus vitamin A' gastruloids elongate and manifest polarized Tbxt and elevated Cdx2 expression similar to the standard 'plus vitamin A' PM gastruloids (Figure 1, F-G). These findings demonstrate that the RA signal is precluded when the culture environment lacks vitamin A. Collectively, these results underscore that the absence of the RA signal is essential for the specification of anterior mesoderm.

To investigate the mesodermal lineages present in AM gastruloids, we conducted single-cell transcriptome analysis. A total of 20,852 cells from 96 gastruloids each from three replicates were sequenced using the 10X Genomics platform. Through dimensional reduction and clustering analysis, we identified and annotated 15 distinct cell types within AM gastruloids (Figure 2A). Similar to PM gastruloids (Mayran et al., 2025; Rekaik et al., 2023; Rosen et al., 2022; Suppinger et al., 2023; van den Brink et al., 2020), mesodermal cell types predominate in AM gastruloids. However, in contrast to PM gastruloids, where the anterior mesoderm constitutes only a minor fraction (6.3%, as reported by (van den Brink et al., 2020)), anterior mesoderm-related clusters together with the prechordal plate cell type accounted for 61.6% of the cells in AM gastruloids (Figure 2B). The posterior mesoderm-related clusters, including somites, node/notochord, and caudal epiblast, comprised only 16.5% of the cells in the AM gastruloids. Based on established gene expression signatures, we identified the anterior mesoderm clusters as cardiopharyngeal mesoderm (*Isl1, Tbx1, Pitx2, Gata6,* and *Fgf10*), pharyngeal mesoderm 1 and 2 (*Isl1, Tbx1, Tcf21, Pitx2, Mesp1,* and *Lhx1*) (Figure 2C, S2A), and anterior paraxial mesoderm (*Tbx1, Meox1, Tcf15, Foxc2, Uncx, Hoxa2,* and *Hoxb2*) (Figure S2C). Notably, we identified one of the clusters as prechordal plate based on the expression of *Otx2, Hesx1, Six3, Sox17, Foxa2* and *Gsc* (Figure 2A, C, D, S2B). In addition to the prechordal plate, we identified a *Foxa2*+ and *Sox17*+ endoderm cluster, a subset of which exhibits pharyngeal identity (*Shh* (Moore-Scott & Manley, 2005)), *Gsc* (P. Thomas & Beddington, 1996), *Otx2* (Ee et al., 2025), *Eya1* and *Six1* (Zou et al., 2006), while a smaller subset is characterized by posterior identity (*Hoxb8* and *Cdx2*) (Figure S2D). The two clusters of differentiated somites, sclerotome and dermomyotome, lack cervical and thoracic Hox gene expression, leading us to consider them representative of differentiated occipital

181 somites (see Figure S4A), which are part of the anterior mesoderm (Vyas et al., 2019;
182 Wehmeyer et al., 2025). These findings clearly demonstrate that the preclusion of RA
183 signaling specifies the anterior mesoderm.

184 The ectoderm formed in AM gastruloids also exhibit anterior characteristics. The *Sox2*+
185 *Sox3*+ neuroectoderm cluster expresses *Hesx1* and *Otx2*, and lacks *Cdx2* and *Hox* gene
186 expression, indicative of forebrain/midbrain identity (Martinez-Barbera et al., 2000;
187 Simeone & Acampora, 2001; Sussel et al., 1999; P. Q. Thomas et al., 2001). It is likely
188 that some of the epiblast cells are induced by the prechordal plate and pharyngeal
189 endoderm to adopt the anterior neural fate. Consistent with the absence of a posterior
190 pole, neuromesoderm progenitor-like population, and posterior neural cell types are
191 absent in AM gastruloids. Therefore, our findings indicate that the preclusion of RA
192 signaling predominantly specifies anterior identity across all germ layers.

193 Based on the expression profiles of *Cdx2*, *Nkx1-2*, *Tbxt*, and *Sox2*, in conjunction with a
194 pluripotent signature, we have designated cluster #8 as caudal epiblast. However, given
195 the low levels of Cdx2 protein and the non-polarized Tbxt expression (Figure 1D), we
196 deduce that a posterior growth zone is not established in AM gastruloids (Gouti et al.,
197 2014; Martin & Kimelman, 2008b; Neijts et al., 2014; Sambasivan & Steventon, 2021).
198 This inference aligns with the observed low elongation index (Figure 1C) and the absence
199 of spinal cord-like cells in the AM gastruloids. Moreover, *Tbx6*, a marker of the posterior
200 paraxial mesoderm (Chapman & Papaioannou, 1998; Javali et al., 2017; Nowotschin et
201 al., 2012; Takemoto et al., 2011) was undetectable by hybridization chain reaction (HCR)
202 in AM gastruloids (Figure 2, C-D). Taken together, these observations suggest that the
203 posterior program is suppressed in the absence of RA signaling.

204 **Preclusion of RA restrains the transition to posterior development**

205 The transcriptome of PM gastruloids corresponds to that of E8.5 mouse embryos (Mayran
206 et al., 2025; Suppinger et al., 2023; van den Brink et al., 2020), which fits with their
207 posterior character. To stage AM gastruloids in relation to mouse embryos, we performed
208 sc-map analysis to project the AM-gastruloid data onto the mouse gastrulation data
209 (Pijuan-Sala et al., 2019). For comparative purposes, we included two PM-gastruloid
210 datasets, one of which encompasses data across a time series (Suppinger et al., 2023;
211 van den Brink et al., 2020). As previously reported, transcriptomically, the 120h PM
212 gastruloids aligned with E8.5 embryos (Figure 2E). Notably, 120h AM gastruloids
213 corresponded to an earlier embryonic stage (Figure 2E); they resembled E7.75 mouse
214 embryos and 96h PM gastruloids. Time series analysis has shown that the trajectory of
215 differentiation in gastruloids mirrors the embryonic temporal developmental sequence
216 (Rosen et al., 2022; Suppinger et al., 2023). Consequently, AM gastruloids model the
217 murine developmental window between E6.5 and E7.75. This observation suggests that

218 the A-P developmental progression is either delayed or restrained in AM gastruloids than
219 in PM gastruloids.

220 To investigate whether retinoic acid (RA) signaling influences the A-P progression, we
221 conducted a comparative analysis of Hox gene expression in AM and PM gastruloids.
222 The temporal collinearity of Hox gene expression functions as a developmental timer.
223 Notably, sc-seq data revealed that the overall Hox gene expression levels were reduced
224 and fewer cells expressed Hox genes in AM gastruloids (Figure 3A). Furthermore,
225 cervical and thoracic Hox genes, such as *Hoxc5* to *Hoxc9*, are expressed in PM
226 gastruloids but are scarcely expressed in AM gastruloids (Figure 3A). Although
227 normalizing and comparing expression levels across datasets presents challenges, our
228 RNA *in situ* hybridization (ISH) data corroborate the findings from the comparative sc-seq
229 data analysis; classical ISH or hybridization chain reaction (HCR) for selected Hox genes
230 confirmed the reduction in Hox gene expression both in terms of levels and the proportion
231 of cells (Figure 3B). To further assess the A-P progression, we assayed the time course
232 of anterior and posterior marker induction in AM versus PM gastruloids. Comparative
233 analysis by RT-qPCR in the earlier time points of AM and PM gastruloids revealed
234 elevated levels of anterior mesoderm genes *Eomes* and *Wnt3*, while the posterior
235 mesoderm regulator *Wnt3a* remained at lower levels throughout in AM gastruloids (Figure
236 3C).

237 As previously reported for PM gastruloids (Beccari et al., 2018; Rekaik et al., 2023),
238 spatial collinearity of Hox genes was also observed in AM gastruloids (Figure 3D). The
239 spatial collinearity in AM gastruloids is depicted in the UMAP, within the A-P
240 developmental gradient of the paraxial mesoderm; the differentiated somitic clusters of
241 sclerotome and dermomyotome express 3' Hox genes, while clusters representing
242 undifferentiated somites, presomitic mesoderm, and caudal epiblast exhibit progressive
243 expression of more 5' Hox genes (Figure 3D). These observations support the anterior
244 predominant identity of AM gastruloids and suggest that, despite the absence of a
245 posterior pole and elongation, AM gastruloids are also organized along the A-P axis.

246 RA functions as an activator of Hox genes (Langston & Gudas, 1994; Nolte et al., 2019).
247 Similarly, Cdx2 serves as a positive regulator of the middle Hox genes of the genomic
248 cluster (Neijts et al., 2017; Rawat et al., 2008; van den Akker et al., 2002), which confers
249 thoracic identity. Since Cdx2 expression is diminished when RA signaling is precluded,
250 the dual block of Hox gene expression may serve as a mechanism for the orderly
251 transition to a posterior developmental program. We propose that the RA signal operates
252 as a temporal regulator; RA signaling expedites the transition to posterior mesoderm
253 development, whereas its preclusion restrains the transition, thereby ensuring a temporal
254 window for anterior mesoderm development.

255

256 **Wnt signaling is attenuated in the absence of RA signaling**

257 The threshold of Wnt signaling paces the transition from anterior to posterior mesoderm
258 development (Dias et al., 2025). Given that our findings suggest a similar role for RA
259 signaling, we investigated whether RA signaling influences the Wnt pathway. To examine
260 this, we compared Wnt signaling levels between AM and PM gastruloids using the *Tcf-*
261 *Lef:mCherry* reporter (Faunes et al., 2013; Ferrer-Vaquer et al., 2010). Reporter
262 expression was reduced in AM gastruloids by 96h (Figure 4A). Assaying by confocal
263 microscopy and flow cytometry, we observed a significant decrease in the reporter signal
264 intensity in AM gastruloids compared with that in PM gastruloids at 120h (Figure 4, A-B).
265 This is striking because both cultures were exposed to the same pulse of Wnt agonist,
266 3μM CHIR99021, for 24h. The results with the reporter assay was corroborated by whole-
267 mount hybridization chain reaction (HCR) for *Axin2*, a target of Wnt signaling (Jho et al.,
268 2002), and *Dkk1*, which encodes a Wnt inhibitor (Niehrs et al., 2001). *Axin2* levels were
269 comparable in AM and PM gastruloids at both 72h and 96h, but it was scarcely detectable
270 in AM gastruloids at 120h (Figure 4C). Conversely, *Dkk1* was widely expressed at
271 elevated levels within AM gastruloids. Notably, at 96 hours, *Axin2* and *Dkk1* RNA were
272 localized at opposite poles (Figure 4C). Collectively, these results demonstrate that Wnt
273 signaling is attenuated in the absence of RA signaling.

274 Next, we investigated whether RA signaling modulated the Nodal pathway. Given that the
275 induction of Nodal/Activin A signaling specifies the anterior mesoderm (Dias et al., 2025),
276 we tested whether Nodal signaling is modulated in the absence of RA. Utilizing
277 *AR8:mCherry*, a Nodal signaling reporter (McNamara et al., 2024; Serup et al., 2012), we
278 observed that Nodal signaling levels were not affected in AM gastruloids compared to
279 those in PM gastruloids (Figure 4, D-E). However, Nodal reporter expression was
280 polarized in AM gastruloids, as reflected by a higher spatial heterogeneity, whereas PM
281 gastruloids displayed a more uniform, dispersed expression pattern (Figure 4D, F). This
282 contrasting spatial pattern of Nodal signaling is reminiscent of observations in mouse
283 embryos. *Nodal* expression was restricted to the posterior epiblast at E6.25. Premature
284 RA exposure disrupts this polarized Nodal expression, leading to ectopic expression in
285 the anterior epiblast (Uehara et al., 2009). The expanded expression is driven by the
286 intronic cis-regulatory element of the Nodal gene, which contains retinoic acid response
287 element (RARE) sites. This observation provides additional evidence for the preclusion
288 of RA signaling in the absence of vitamin A in the milieu.

289 The polarized Nodal signaling in the E6.25 mouse embryo is essential for protecting the
290 anterior pole from posteriorization (Uehara et al., 2009). This is critical to create a Nodal-
291 inhibited anterior pole, which promotes anterior mesoderm differentiation (Nandkishore
292 et al., 2018). However, the significance of the spatial pattern of Nodal signaling for
293 specifying anterior mesoderm within the primitive streak remains unknown.

294 ***Eomes* is necessary to suppress the posterior mesoderm fate**

295 Wnt signaling activates the mesodermal program by targeting the T-box transcription
296 factors, Eomes and Tbxt, which regulate the mesoderm gene network. To investigate the
297 interaction between RA signaling and the Wnt-driven mesodermal network, we examined
298 the function of *Eomes* and *Tbxt* in the absence of RA signaling. First, we studied the role
299 of *Eomes*. Loss of *Eomes* function in mouse embryos results in failure of epithelial-to-
300 mesenchymal transition in the primitive streak (Arnold et al., 2008; Russ et al., 2000), and
301 *Eomes*-null mutant mESCs are unable to differentiate into cardiomyocytes, indicating a
302 failure in specifying anterior mesodermal fate (Costello et al., 2011). We generated AM
303 gastruloids (minus vitamin A gastruloids) using *Eomes*$^{-/-}$ mESCs and performed
304 phenotypic analyses. Strikingly, unlike wild type AM gastruloids, *Eomes*$^{-/-}$ AM gastruloids
305 expressed elevated levels of Cdx2; similarly to PM gastruloids, expression of Cdx2 and
306 Tbxt was polarized (Figure 5, A-B). This is consistent with the recently reported
307 observation that the *Eomes*$^{-/-}$ gastruloids generated through Activin A induction also
308 initiate Cdx2 expression, whereas wild type Activin A gastruloids do not express Cdx2
309 (Wehmeyer et al., 2025). Although we observed variability across experiments, *Eomes*$^{-/-}$
310 AM gastruloids often displayed elongation. These observations indicate that the posterior
311 growth zone is established even in the absence of RA signaling when *Eomes* function is
312 lost.

313 To further investigate the phenotype, we conducted single-cell sequencing of *Eomes*$^{-/-}$
314 AM gastruloids. A total of 10,991 cells from 144 gastruloids pooled from two replicates
315 were sequenced. UMAPs generated through dimension reduction and clustering analysis
316 allowed the identification of 15 distinct cell types present in the mutant AM gastruloids
317 (Figure 5C). Four anterior mesoderm clusters were identified: cardiac mesoderm,
318 pharyngeal mesoderm, and anterior paraxial mesoderm 1 and 2 (Figure 5C, S3A).
319 Notably, in comparison to the wild type, *Eomes* mutant AM gastruloids exhibited an
320 increased proportion of posterior mesoderm cell types (Figure 5D, S3B). Unlike in the wild
321 type, neuromesoderm progenitors, a major source of posterior paraxial mesoderm and
322 spinal cord, were specified in the mutant gastruloids (Figure 5C, S3C). Furthermore, the
323 posterior mesoderm clusters appeared to exhibit elevated levels of thoracic Hox gene
324 expression relative to the wild type (Figure S3B, see also S4B). This posterior phenotype
325 aligns with the increased, polarized Cdx2 expression and elongation observed in the
326 mutants, and highlights the function of *Eomes* in inhibiting the posterior fate.

327 The sclerotome and dermomyotome clusters exhibit anterior/occipital identity in wild type
328 AM gastruloids. In *Eomes*$^{-/-}$ AM gastruloids, these clusters show expression of thoracic
329 *Hox* genes, such as *Hoxc5*, *Hoxc8* and *Hoxb8* (Figure S3B, S4B), and therefore they are
330 of thoracic identity. We interpret the ‘posteriorized’ phenotype as an 'anterior shift in the
331 boundary' of thoracic Hox genes into the cervical axial level. Despite the specification of
332 the cardiac lineage and the detection of low levels of Isl1 RNA, Isl1 protein expression is

333 reduced or undetectable in *Eomes*$^{-/-}$ AM gastruloids (Figure S3A, D; (Costello et al.,
334 2011)). These findings are consistent with the role of Eomes in restricting the function of
335 Tbxt to curb posterior fate (Schüle et al., 2023).

336 To further address the differences in the cell types specified between wild type and
337 *Eomes*$^{-/-}$ AM gastruloids, we integrated the wild type and *Eomes*$^{-/-}$ datasets and
338 generated a UMAP (Figure 5E). The clusters in the UMAP of the integrated dataset were
339 annotated based on marker gene expression. Comparison of the distribution of *Eomes*$^{-/-}$
340 cells with those of wild type shows broadly similar composition of both types of AM
341 gastruloids (Figure 5F). We observed an increased representation of presomitic
342 mesoderm and sclerotome in the *Eomes*$^{-/-}$ (Figure 5F; see also Figure 6E). Moreover,
343 the anterior mesoderm cell populations in the mutant AM gastruloids appear to be
344 'posteriorized'. Analysis of differential expression of select genes showed diminished
345 expression of anterior markers such as *Gsc, Hesx1*, and *Isl1*, and higher levels of
346 posterior paraxial mesoderm markers, such as *Meox1, Meox2, Foxc2, Uncx* and *Tbx6* in
347 the anterior mesoderm derivatives (Figure 5G). Notably, the posteriorization in the
348 absence of *Eomes* function is evidenced by the preferential posterior localization of
349 *Eomes*$^{-/-}$ cells in chimeric AM gastruloids generated by mixing GFP-labelled mutant and
350 wild type cells (Figure 5H). Based on our findings, we conclude that the absence of RA
351 signaling is permissive for anterior identity specification. However, anterior mesoderm
352 specification is dependent on *Eomes* function. When RA signaling is precluded, *Eomes*
353 functions to prevent the precocious posterior program activation to ensure orderly A-P
354 developmental progression.

355 ***Tbxt* suppresses posterior fate in the absence of RA**

356 In contrast to *Eomes* mutants, anterior mesoderm specification and differentiation remain
357 unaffected in *Tbxt* mutant mouse embryos; however, posterior mesoderm development
358 is disrupted (Herrmann, 1991; Nandkishore et al., 2018). While *Tbxt* is expressed in the
359 anterior mesoderm progenitors, its function in their specification is unclear. We
360 investigated the function of *Tbxt* in anterior mesoderm development using AM gastruloid
361 model. Unexpectedly, we observed elevated Cdx2 expression in *Tbxt*$^{-/-}$ AM gastruloids
362 (Figure 6A) compared to the wild type. Although Cdx2 levels are increased, *Tbxt*$^{-/-}$ AM
363 gastruloids do not elongate; they retain a spherical morphology. The activation of the
364 posterior factor Cdx2 in *Tbxt*$^{-/-}$ gastruloids, despite the absence of RA signaling, presents
365 a paradox given the critical role of *Tbxt* in the development of posterior mesoderm.

366 To investigate this unexpected mutant phenotype and the role of *Tbxt* in anterior
367 developmental program, we conducted single-cell sequencing on *Tbxt*$^{-/-}$ AM gastruloids.
368 A total of 13,960 cells from two experimental replicates of 96 gastruloids each were
369 sequenced. UMAP visualization enabled the identification of 13 distinct cell types within
370 *Tbxt*$^{-/-}$ AM gastruloids (Figure 6B). Consistent with existing literature, posterior paraxial

371 mesoderm and its derivatives were nearly absent in 120h *Tbxt*$^{-/-}$ AM gastruloids. As
372 expected, the anterior mesoderm cell types were specified; however, unlike the wild type
373 AM and *Eomes* mutant AM gastruloids, *Tbxt*$^{-/-}$ AM gastruloids were predominantly
374 composed of neural cells (46.1%) (Figure 6, B-C), with a reduced proportion of mesoderm
375 (25%). The integration of our wild type, *Eomes*$^{-/-}$ and *Tbxt*$^{-/-}$ sc-seq datasets showed that
376 *Tbxt*$^{-/-}$ AM gastruloids are relatively enriched for early cardiac mesoderm (Figure 6, D-E).
377 This analysis also highlights the increased presence of posterior neural cells and epiblast-
378 like cells uniquely in *Tbxt*$^{-/-}$ (Figure 6, D-E). These observations highlight the key role of
379 *Tbxt* in mesoderm development.

380 Another striking phenotype of *Tbxt*$^{-/-}$ AM gastruloids is that the neural lineages were of
381 posterior identity, unlike those in the wild type. The largest cluster in the UMAP was
382 composed of spinal cord cells expressing *Pax6, Sox2,* and *Nkx1-2* (Figure 6B, S5). Two
383 of the clusters corresponded to the neuromesoderm progenitors. Moreover, instead of the
384 forebrain/midbrain neural cells specified in the wild type, *Tbxt*$^{-/-}$ AM gastruloids contained
385 a hindbrain-like cluster expressing *Krox20* and *Phox2* (Figure 6B, S5). Hox gene
386 expression further corroborated the posterior character of the mutant neuroectoderm
387 (Figure S4C, S5). Therefore, a notable phenotype of *Tbxt*$^{-/-}$ AM is the induction of
388 posterior fates, specifically the neuromesoderm progenitors and spinal cord, even in the
389 absence of the RA signal. The expression of Cdx2 protein observed in *Tbxt*$^{-/-}$ gastruloids
390 appears predominantly to be from the posterior neural cell types, spinal cord and
391 neuromesoderm (Figure S5). Therefore, our findings show that the loss of *Tbxt* in
392 conjunction with the absence of RA signalling drives posterior fate. Indeed, when we
393 combined wild type and tdTomato-labelled *Tbxt*$^{-/-}$ mESCs, the resulting chimeric AM
394 gastruloids exhibited elongation and polarized Cdx2 expression. In this context, the
395 mutant cells predominantly localized at the posterior pole (Figure 6F), indicating that the
396 conditions resulting from the loss of *Tbxt* and the absence of RA facilitated the
397 development of posterior identity. Therefore, our findings demonstrate that Cdx2
398 expression and posterior fate are activated when *Tbxt* and the RA signal are absent.

399 **Wnt-Cdx2 posterior developmental module is suppressed in the absence of RA**

400 When projected on to the single-cell transcriptomic data of mouse gastrula, the
401 transcriptome of both *Eomes*$^{-/-}$ and *Tbxt*$^{-/-}$ AM gastruloids mapped partially to E8.5
402 embryo, further supporting the specification of posterior fates in the mutants (Figure 7A).
403 To address the mechanism underlying the elevated expression of Cdx2 and the
404 specification of posterior fate in T-box mutant gastruloids, despite the absence of retinoic
405 acid (RA) signaling, we evaluated the levels of Wnt signaling in these mutant gastruloids.
406 Canonical Wnt signaling is a principal regulator of Cdx2 (Chawengsaksophak et al., 2004;
407 Wang & Shashikant, 2007) within the posterior axial progenitor pool. *Wnt3* is activated,
408 but *Wnt3a* is suppressed by Eomes (Wehmeyer et al., 2025). In contrast, Tbxt and Wnt3a
409 positively regulate each other through feedback mechanisms (Martin & Kimelman, 2008a;

410 Wehmeyer et al., 2025; Yamaguchi, Yoshikawa, et al., 1999). First, we assessed the
411 expression of *Wnt3* and *Wnt3a* in our sc-seq datasets (Figure 7B). In both the wild type
412 and *Eomes*$^{-/-}$, *Wnt3* and *Wnt3a* expression is confined primarily to the caudal epiblast,
413 node/notochord or neuromesoderm cell clusters. Interestingly, the expression of *Wnt3*
414 appeared derepressed in *Tbxt*$^{-/-}$ gastruloids, and it was widely expressed in the anterior
415 mesoderm populations, in addition to the caudal epiblast-like population. As expected,
416 *Wnt3a* expression was diminished in *Tbxt*$^{-/-}$ gastruloids (Figure 7B). The positive
417 feedback loop of *Tbxt* and *Wnt3a* explains the *Wnt3a* downregulation in the mutants. This
418 observation suggests that *Tbxt* suppresses *Wnt3* expression in the anterior mesoderm
419 lineage.

420 To assay Wnt signaling in the mutant gastruloids, we generated chimeric AM gastruloids
421 by seeding a 50:50 mixture of *Tcf-Lef:mCherry* and *Eomes*$^{-/-}$ or *Tcf-Lef:mCherry* and
422 *Tbxt*$^{-/-}$ mESCs. If the Wnt ligands are upregulated in the mutant cells, the wild type
423 reporter cells within the chimera will provide the signaling read-out. Through confocal
424 imaging and flow cytometry, we observed an increase in Wnt reporter expression in both
425 *Eomes*$^{-/-}$ and *Tbxt*$^{-/-}$ chimeric gastruloids compared to non-chimeric wild type (*Tcf-*
426 *Lef:mCherry*) AM gastruloids (Figure 7, C-D). These findings support the possibility that
427 the enhanced Cdx2 expression in the mutants is due to the elevated Wnt signaling.

428 To determine whether the activation of Cdx2 can be attributed to increased Wnt signaling,
429 we investigated the dependency of Cdx2 activation on Wnt signaling. PM gastruloids were
430 treated with Xav939, a tankyrase inhibitor that suppresses the Wnt pathway, and Cdx2
431 levels were assessed by immunostaining. We observed that inhibition of Wnt signaling
432 downregulated the expression of Cdx2 in wild type PM gastruloids (Figure 7E). Moreover,
433 Xav939-treated PM gastruloids showed limited elongation and non-polar Tbxt expression
434 akin to wild type AM gastruloids. These observations support the hypothesis that elevated
435 Wnt signaling induces the activation of the Wnt-Cdx2 module, and that the de-repression
436 of the Wnt-Cdx2 module underlies the accelerated acquisition of posterior fate in T-box
437 factor mutant gastruloids, even in the absence of RA signaling.

438 To further probe the role of RA signaling in regulating Cdx2, we tested the expression of
439 Cdx2 in the Activin A-based gastruloids. High concentrations of Activin A (ActA), an
440 activator of the Nodal signaling pathway, drives anterior mesoderm specification (Dias et
441 al., 2025). We assayed Cdx2 expression in high ActA gastruloids in presence/absence of
442 vitamin A. Cdx2 is expressed in fewer cells in ActA gastruloids generated in the presence
443 of vitamin A compared to PM gastruloids. However, without vitamin A, ActA gastruloids
444 display a further reduction in Cdx2 levels (Figure 7F). This suggests that the preclusion
445 of RA signaling is critical for effective suppression of Wnt-Cdx module and thus, the
446 posterior fate.

447

## Discussion:

The mechanisms underlying the sequential development of the animal body plan from the anterior to the posterior are beginning to be elucidated. Our research indicates that RA signaling plays a crucial role in facilitating the A-P developmental transition. Specifically, we propose that the absence of RA signaling during early gastrulation attenuates Wnt signaling, permitting the specification of anterior identity, including the anterior mesoderm. The Wnt-Cdx module is not activated at low Wnt signal thresholds, preventing premature activation of the posterior program. The subsequent activation of RA signaling during later gastrulation promotes increased Wnt signaling, which stabilizes the Wnt-Cdx module, causing a shift from the anterior to the posterior developmental program. Our findings indicate that RA signaling is integral to the regulatory logic governing the orderly A-P progression. The model emerging from recent research posits that the Nodal-Eomes-Wnt3 axis facilitates anterior mesoderm development, whereas the opposing Wnt3a-Tbxt axis promotes posterior mesoderm fate (Dias et al., 2025; Wehmeyer et al., 2025). Based on the evidence in the literature and our findings, we propose that RA signaling regulates the developmental transition from anterior to posterior mesoderm by impinging on the core anterior (Nodal-Eomes) and posterior (Wnt-Tbxt) networks (Figure 8).

*Eomes* and *Tbxt* are expressed in early streak mouse embryos, where they attenuate Wnt signaling by repressing *Wnt3a* and *Wnt3* expression, respectively (Wehmeyer et al., 2025). During the late streak stage, *Eomes* levels decrease, relieving its restriction on *Tbxt* function (Schüle et al., 2023), leading to elevated *Wnt3a* expression through positive feedback with *Tbxt* (Evans et al., 2012; Martin & Kimelman, 2008a; Schwaiger et al., 2022; Turner et al., 2014; Yamaguchi, Takada, et al., 1999). This may lead to low Wnt signaling in early streak embryos and heightened Wnt signaling in late streak embryos. Since Cdx2 is a Wnt signal target (Amin et al., 2016), we speculate that high Wnt signal threshold induces Cdx2 expression, activating the posterior Wnt-Cdx module. Despite the absence of RA signaling, Wnt signaling was elevated in both *Eomes* and *Tbxt* null mutants, correlating with *Wnt3a* upregulation in *Eomes*$^{-/-}$ and sustained *Wnt3* expression in *Tbxt*$^{-/-}$. In both the cases, a Cdx2+ posterior growth zone was formed. We propose that deregulation of Wnt signaling in the mutants causes stabilization of the Wnt-Cdx module resulting in posterior fate specification. These findings underscore the central role of Wnt signaling, and suggest that RA functions by gating the Wnt signaling in A-P developmental progression.

RA signaling has a conserved role in regulating the collinear expression of *Hox* genes across Chordata (Schubert et al., 2006). RA signaling activates Cdx factors (Amblard et al., 2025; Houle et al., 2000), implicating RA in the activation of mid-cluster Hox genes via Cdx factors (Deschamps & van Nes, 2005). Moreover, several studies have demonstrated that RA signalling regulates patterning of the posterior body (Abu-Abed et

al., 2001; Hennessy et al., 2023; Iulianella et al., 1999; Kessel & Gruss, 1991). Thus, the role of RA in patterning the posterior body following the transition to posterior program is well established. In this study, we have demonstrated that the preclusion of RA signaling is essential for anterior identity specification. In this context, the importance of RA signaling is underscored by the striking phenotype observed in *Cyp26a1/2/3*$^{-/-}$ triple mutant embryos. Failure to restrict the influence of maternal RA in early streak mouse embryos leads to ectopic *Tbxt* expression in the anterior region. This has been interpreted as axis duplication (Uehara et al., 2009). Given our findings, we reinterpret the *Cyp26a*$^{-/-}$ phenotype as also reflecting the 'posteriorization' of anterior mesoderm. Taking this together with our findings, we conclude that the inhibition of RA signaling is essential for safeguarding anterior development from inappropriate posterior differentiation. We propose that the regulation of RA signaling, from its suppression to activation during the early to late phases of gastrulation, is key to regulating the orderly A-P developmental transition. Addressing how RA signalling itself is regulated, in the switch from an RA-precluded to an RA-active state, will further elucidate the anterior-to-posterior developmental transition.

The Wnt and Nodal pathways play a fundamentally conserved role in A-P axis patterning (Arnold & Robertson, 2009; Hikasa & Sokol, 2013; Robertson, 2014; Tian & Meng, 2006). The RA signaling pathway is similarly conserved across eumetazoans (Rhinn & Dollé, 2012). However, RA signaling appears to have been co-opted for patterning the overall A-P body axis later in evolutionary history, suggesting that it is a chordate innovation (Cañestro et al., 2006; Marlétaz et al., 2006). We have demonstrated that Wnt signaling is central and that RA signaling gates Wnt signaling to regulate the axial mesoderm patterning. Taking this together with the later recruitment of RA signaling in phylogeny, we propose that RA signaling functions to reinforce the core Nodal/Wnt mechanism regulating the orderly developmental transition. With the complexity of the animal body increasing through evolution, the co-option of RA signaling could have reinforced the A-P patterning mechanisms by making it robust and resilient to noise.

515 **Material and methods**

516 **Lead contact**

517 Further information and requests for resources and reagents should be directed to and
518 will be fulfilled by the Lead Contact, [Ramkumar Sambasivan]
519 ([ramkumars@labs.iisertirupati.ac.in]).

520 **Materials availability**

521 Cell lines generated in this study are available upon request.

522 **Data and code availability**

523 Code for the single cell analysis can be found in (https://github.com/gatocor/project-
524 vitamin-A)

525 **Experimental model and subject details**

526 **Mouse embryonic stem cells**

527 All cell lines used are listed in methods table 1 below. Gastruloids were generated from
528 E14Tg2a and E14Tg2a-GFP mouse embryonic stem cells (mESCs). We have also used
529 signaling pathway reporter lines such as Tcf/Lef-mCherry and AR8-mCherry, and RARE-
530 d2-eGFP. *Eomes*$^{-/-}$ and *Tbxt*$^{-/-}$ mESCs were generated in-house using the E14Tg2a line.
531 *Eomes*$^{-/-}$*-GFP* and *Tbxt*$^{-/-}$*-tdTomato* were used for loss of function studies.

532 **Methods table 1**

| Cell lines | Source | Reference |
|---|---|---|
| E14Tg2a | P. Chandra Shekar | (Doetschman et al., 1987) |
| E14Tg2a-GFP | Generated for this study | |
| Tcf-lef mCherry | Alfonso Martinez Arias | (Faunes et al., 2013; Serup et al., 2012) |
| AR8 mCherry | Alfonso Martinez Arias | (Serup et al., 2012) |
| RARE-d2-eGFP | Generated for this study | |
| *Tbxt*$^{-/-}$ | Generated for this study | |
| *Eomes*$^{-/-}$ | Generated for this study | |
| *Eomes*$^{-/-}$*-GFP* | Generated for this study | |
| *Tbxt*$^{-/-}$*-tdTomato* | Generated for this study | |

533

534 **METHOD DETAILS**

535 **Cell culture**

536 Mouse embryonic stem cells (mESCs) were maintained at 37°C and 5% CO2 on 0.1%
537 gelatin-coated 35-mm tissue culture dishes. Glasgow Minimum Essential Medium
538 (GMEM) supplemented with 10% fetal bovine serum (FBS), 1× non-essential amino
539 acids, 2mM GlutaMAX, 1× penicillin–streptomycin, 0.1mM β-mercaptoethanol, and
540 1000U/mL leukemia inhibitory factor (LIF; ESGRO) was used as the growth medium.
541 Cells were passaged every other day at a confluency of ≤60%. For passaging, the
542 medium was removed, the cells were washed with 1mL of PBS, and then dissociated with
543 400μL of TrypLE for 3.5 min at 37 °C. The reaction was quenched with 1.6mL of growth
544 medium, and the cells were triturated 15–20 times to obtain a single-cell suspension.
545 One-tenth of the suspension was transferred to a fresh gelatin-coated dish containing
546 1.8mL of growth medium. The references for media and culture reagents and plasticware
547 are listed in methods tables 2 and 3.

548 **Methods table 2**

| mES growth media | Concentration | Catalogue number | Source |
|---|---|---|---|
| GMEM | Make up to the required volume | 11710035 | Gibco |
| Fetal bovine serum | 10% | RM9952 OR RM10686 | Gibco |
| MEM non-essential amino acid | 1X | 11140-050 | Gibco |
| Glutamax (100X) | 1X | 35050-061 | Gibco |
| Penicillin/ Streptomycin (100X) | 1X | 15070063 | Gibco |
| β-mercaptoethanol | 100 μM | 21985023 | Gibco |
| Leukemia inhibitory factor (LIF) | $10^3$ units (1:10000 dilution) | ESG1107 | Merck |

549 **Methods table 3**

| Cell culture | Catalogue number | Source |
|---|---|---|
| PBS, pH 7.4 | 10010023 | Gibco |
| TrypLE™ Express Enzyme (1X), Phenol Red | 12605010 | Gibco |

| Gelatin | TC041 - 100G | Himedia |
|---|---|---|
| 35-mm tissue culture dish | 353001 | Corning |
| 60mm tissue culture dish | 353002 | Corning |
| 96-well U bottom dish, non-treated | 34296 | Genetix |
| 6-well low attachment dish | 3471 | Corning |

550 **Gastruloid culture**

551 The mESCs were preconditioned by subculturing in 35-mm dishes on growth medium
552 supplemented with 1μM PD0325901 (MEK inhibitor) and 3μM CHIR99021 (GSK3
553 inhibitor) for 24h prior to gastruloid formation. Following the 2i pre-treatment, mESCs
554 were washed twice with 1mL PBS and dissociated with TrypLE (similar to the cell passage
555 protocol). The single-cell suspension was transferred to a 15mL tube and centrifuged at
556 1000 rpm for 3 min in a swing-bucket centrifuge. The supernatant was removed, and the
557 cells were washed twice with 2mL PBS. Pelleted cells were resuspended in N2B27
558 medium, and viable cell numbers were determined using a hemocytometer. N2B27
559 medium was prepared by combining 24.1mL DMEM/F12, 24.1mL Neurobasal medium,
560 250μL N2 supplement, 500μL B27 supplement, 500μL L-glutamine, 500μL penicillin–
561 streptomycin, and 50μL β-mercaptoethanol to a final volume of 50mL. For posterior
562 mesoderm (PM) gastruloids, B27 supplement with vitamin A was used, whereas for
563 anterior mesoderm (AM) gastruloids, B27 without vitamin A was used.

564 Aggregates were generated by seeding 300 cells per well in 40μL N2B27 medium in non-
565 tissue-culture-treated U-bottom 96-well plates. After 48h, gastruloids were induced with
566 3μM CHIR99021 in 150μL N2B27. At 72h and 96h, the spent medium was replaced with
567 150μL of fresh N2B27. For endpoint analysis, gastruloids were collected at 120h. The
568 references for media and other reagents are listed in methods tables 4 and 5.

569 **Methods table 4**

| N2B27 media | Working Concentration | Catalogue number | Source |
|---|---|---|---|
| Neurobasal medium | 48.20% | 21103049 | Gibco |
| DMEM-F12 (HEPES) | 48.20% | 11330032 | Gibco |
| N2 Supplement (100X) | 1X | 17502048 | Gibco |
| B27 with vitamin A (50X) | 1X | 17504044 | Gibco |
| B27 without vitamin A (50X) | 1X | 12587010 | Gibco |

| | | | |
|---|---|---|---|
| L-glutamine (100X) | 1X | 25030081 | Gibco |
| Penicillin/ Streptomycin (100X) | 1X | 15070063 | Gibco |
| β-mercaptoethanol | 100μM | 21985023 | Gibco |

570 **Methods table 5**

| Growth factors and inhibitors | Concentration | Catalogue number | Source |
|---|---|---|---|
| CHIR99021 (GSK3 inhibitor) | 3μM | 4423/10 | Tocris |
| CHIR99021 (GSK3 inhibitor) | 3μM | SML1046-25MG | Merck |
| PD0325901 (MEK inhibitor) | 1μM | 100-0248 | Stemcell Technologies |
| Activin A | 100ng/ml | 338-AC-050 | R&D Systems |
| Xav939 | 5μM | X3004-5MG | Sigma |
| Fgf10 | 50ng/ml | 345-FG-025 | R&D Systems |
| IGF1 | 2ng/ml | 250-19-10 | Peprotech |

571 **Cardiac organoid culture**

572 After 120h, the AM gastruloids were transferred to a 6-well low attachment plate and kept
573 on a shaker at 40-60rpm and continued in the gastruloid culture medium supplemented
574 with Fgf10 (50ng/ml) and IGF-1 (2ng/ml). For endpoint analysis, gastruloids were
575 collected at 192h.

576 **Immunostaining and imaging**

577 Gastruloids were collected into individual wells of a 48-well plate or 24-well plate, rinsed
578 twice with PBS to remove residual medium, and fixed in 4% paraformaldehyde (PFA) for
579 2h at 4 °C. Following fixation, gastruloids were washed three times with PBS (20 min
580 each at room temperature) and stored at 4 °C until further processing. Gastruloids were
581 permeabilized and blocked in PBS-FT (PBS containing 10% FBS and 0.25% Triton X-
582 100) for 1h at room temperature. All staining steps were performed on an orbital shaker.
583 Primary antibodies were diluted in PBS-FT at the indicated concentrations, and
584 gastruloids were incubated for 24h at 4 °C. Samples were then washed three times with
585 PBS-FT (20 min each) and incubated with secondary antibodies, also diluted in PBS-FT,
586 for 24h at 4 °C. After staining, gastruloids were washed three additional times with PBS-
587 FT (20 min each), rinsed with PBS, and stored at 4 °C until imaging.

588 Gastruloids were mounted in 100% glycerol on coverslip-bottom 35-mm dishes. Confocal
589 images were acquired using an Olympus FV3000 microscope with 10× or 20× objectives.
590 Z-stacks were captured using system-optimized step sizes.

591 Post-acquisition image processing was performed in Fiji (ImageJ). Fluorescence
592 channels were split, and maximum intensity projections were generated from the acquired
593 Z-stacks for preparing the images for the figures. For quantification of fluorescence
594 intensity along the anterior-posterior (A-P) axis, a midline was drawn along the length of
595 each gastruloid using the line tool and fitted to a spline. Intensity values along the midline
596 were extracted using the "Plot Profile" function (Cmd+K), exported to Excel, and plotted
597 in R. For elongation index quantification, the major axis was defined as the length of the
598 midline, and the minor axis was measured as the diameter of the largest inscribed circle
599 within the gastruloid.

600 The primary antibodies used are listed in table 6.

601 **Methods table 6**

| Antibodies | Dilution | Catalogue number | Source |
|---|---|---|---|
| Tbxt | 1:500 | sc-17743 | SantaCruz Biotechnology |
| Tbxt | 1:200 | ab209665 | Abcam |
| Eomes | 1:100 | ab23345 | Abcam |
| Cdx2 | 1:5 | AM392-5M | BioGeneX |
| Isl1 | 1:100 | 40.2D6 | DSHB |
| GFP | 1:1000 | ab13970 1 | Abcam |
| mCherry | 1:250 | ab183628 | Abcam |
| Sox2 | 1:250 | sc17320 | SantaCruz Biotechnology |
| Myl14 (MF20) | 1:100 | MF20 - AB2147781 | DSHB |

602 ***in situ* hybridization (ISH)**

603 **Probe synthesis:**

604 Antisense RNA probes were generated either from linearized plasmid templates or from
605 PCR-amplified fragments. For plasmid-based templates, vectors containing the desired
606 insert were linearized, and *in vitro* transcription was performed using 1µg of linearized
607 DNA with the DIG RNA Labeling Kit (Roche, Cat. No. 11175025910), according to the

608 manufacturer's instructions. The reaction mixture contained 1mM each of ATP, CTP, and
609 GTP, 0.65mM UTP, and 0.35mM DIG-11-UTP and was incubated for 2h at 37°C.
610 Template DNA was then digested with DNase I, and the reaction products were purified
611 using Bio-Rad Micro Bio-Spin 30 chromatography columns. Probe integrity was verified
612 by agarose gel electrophoresis, and concentrations were determined by a NanoDrop
613 spectrophotometer.

614 For probes generated from PCR-amplified DNA templates, cDNA was synthesized from
615 mouse embryo RNA corresponding to a developmental stage known to express the gene
616 of interest, and cDNA was synthesized. Gene-specific primers were designed to amplify
617 the desired fragment, with a T7 or T3 RNA polymerase binding site appended to the 5′
618 end of the forward primer. The purified PCR amplicon was then used directly as a
619 template for *in vitro* transcription, as described above. Aliquots of the purified probes
620 (typically ~200ng per reaction were stored at -20°C until use.

621 **Whole-mount ISH on gastruloids:**

622 Gastruloids were collected in 4-well dishes. Media was removed, and gastruloids were
623 washed with PBS before fixing in 4% paraformaldehyde (PFA) at 4°C overnight. Three
624 washes in PTW (PBS + 0.1% Tween-20) were given to remove PFA. Samples were
625 dehydrated through a methanol/PTW series (25%, 50%, 75%, 100%) and stored in 100%
626 methanol at –20°C. On the day of performing in-situ hybridization, samples were
627 rehydrated in methanol/PTW series (75%, 50% 20%, 0%). No Proteinase K treatment
628 was done prior to hybridization. Prehybridization was performed for 1h at 70°C in
629 hybridization mix (50% formamide, 1.3× SSC (pH 5), 5mM EDTA, 0.5% CHAPS, 0.2%
630 Tween-20, 100µg/mL heparin, and 50µg/mL yeast RNA). Hybridization was carried out
631 overnight at 70°C with ~100ng of DIG-labeled RNA probe in a pre-warmed hybridization
632 mix. Post-hybridization washes were performed at 70°C (2 × 30 min in hybridization mix,
633 followed by 1 × 20 min in a 1:1 hybridization mix/MABT solution). Gastruloids were then
634 washed three times in MABT (Maleic acid buffer + 0.1% Tween-20) and blocked for 1h in
635 MABT containing 2% Roche blocking reagent and 20% heat-inactivated goat serum. Anti-
636 DIG-AP antibody (Roche) was added at a 1:2000 dilution in the blocking buffer and
637 incubated overnight at 4°C. Following three washes in MABT and a 24h room-
638 temperature wash, gastruloids were rinsed twice in NTMT buffer and stained in BM Purple
639 (Roche) at room temperature until color development was complete. Staining reactions
640 were stopped by washing three times in PTW. Gastruloids were post-fixed overnight in
641 4% PFA at 4°C and stored long-term in 0.5% PFA at 4°C. Stained gastruloids were
642 imaged on a 35-mm dish in PBS using a stereo zoom microscope. The reagent list is
643 provided in table 7.

644

645 **Methods table 7**

| Components of ISH Hybridization Buffer | Concentration | Stock Concentration | Catalogue number | Source |
|---|---|---|---|---|
| Formamide | 50% | - | 47671-1L-F | Sigma |
| SSC (pH 5) | 1.3x | 20x | S6639-1L | Sigma |
| EDTA | 5mM | 0.5M, pH 8.0 | 15575020 | Gibco |
| Yeast RNA | 50µg/ mL | 10mg /mL | 10109223001 | Roche |
| CHAPS | 0.5% | 10% | C3023-5G | Sigma |
| Tween-20 | 0.2% | 10% | P1379 | Sigma |
| Heparin | 100µg/ mL | 50mg/ mL | H3149 | Sigma |

646 **Hybridization Chain Reaction** (HCR; RNA Fluorescence *in situ* Hybridization):

647 HCR RNA-FISH was performed using the Molecular Instruments HCR v3.0 kit (Molecular
648 Instruments, Los Angeles, CA) according to the manufacturer's instructions, with minor
649 modifications optimized for gastruloids and mouse embryos. Briefly, samples were fixed,
650 dehydrated, and rehydrated similar to ISH as mentioned above. Prior to hybridization,
651 samples were equilibrated in HCR hybridization buffer (Molecular Instruments). The pre-
652 hybridization solution was then removed and replaced with fresh hybridization buffer
653 containing probe sets targeting the genes of interest (typically at a final probe
654 concentration of 4nM) and incubated overnight at 37°C. Following hybridization, excess
655 probes were removed by a series of washes in pre-warmed HCR wash buffer and 5×
656 SSCT (saline-sodium citrate with 0.1% Tween-20), as per the Molecular Instruments
657 protocol.

658 For signal amplification, samples were equilibrated in amplification buffer and then
659 incubated overnight at room temperature in amplification buffer containing pre-annealed
660 fluorescently labeled HCR hairpins (typically 60nM each). Prior to use, hairpins were
661 snap-cooled by heating to 95°C for 90s followed by slow cooling to room temperature for
662 30 min in the dark.

663 After amplification, samples were washed extensively in 5× SSCT to remove unbound
664 hairpins and then counterstained with Hoechst (1µg/ml) for 48h at 4°C. Imaging was
665 performed using a confocal laser scanning microscope (Olympus FV3000) with identical
666 acquisition settings across conditions.

667

668

669 **Single-cell RNA sequencing**

670 Single-cell suspensions were prepared from gastruloids derived from wild type (n = 3
671 biological replicates), *Eomes* mutant (n = 2), and *Tbxt* mutant (n = 2) lines. For each
672 experiment, ~96 gastruloids were collected in a 35-mm dish and washed once with PBS.
673 Gastruloids were dissociated with 700µL TrypLE Express for 5 min at 37°C and quenched
674 with 3.2mL FBS-containing growth medium. The suspension was gently triturated to
675 obtain a single-cell suspension and transferred to a 15mL tube. The suspension was
676 diluted with 10mL PBS, and cells were pelleted by centrifugation (1000 rpm, 3 min). The
677 pellet was resuspended in PBS supplemented with 1% BSA, and cell concentration and
678 viability were determined using a hemocytometer. The viability was ~96% in the cell
679 suspension.

680 Single-cell RNA sequencing libraries were prepared using the Chromium Next GEM
681 Single Cell 3′ Library & Gel Bead Kit v3.1 (10x Genomics) according to the manufacturer's
682 instructions. For each condition, approximately 8,000 dissociated cells were loaded per
683 channel. Libraries were sequenced on an Illumina NovaSeq 6000 (paired-end, 28 × 91
684 bp), targeting ~50,000 reads per cell. The mean number of reads per cell ranged from
685 20,000 to 50,000 across samples. Raw data were processed using Cell Ranger v9.0.0
686 (10x Genomics) with the mm10 reference genome (refdata-gex-mm10-2020-A).

687 All analyses were performed using Scanpy (Wolf et al., 2018) unless otherwise stated.

688 Quality control was performed independently for each condition and replicate. Standard
689 QC metrics were computed, including the total number of transcripts per cell, the number
690 of detected genes, and the fraction of mitochondrial reads. Thresholds for filtering low-
691 quality cells were determined heuristically from the distributions of these metrics to
692 remove cells with low RNA content, stressed or dying cells, empty droplets, and potential
693 doublets. Doublet detection was refined using Scrublet (Wolock et al., 2019). The doublet
694 score threshold was chosen heuristically based on UMAP representations to exclude
695 regions enriched for high doublet scores while maintaining biological integrity across
696 batches. Outlier cells with abnormally high mean distances from their k-nearest neighbors
697 were also excluded. Inclusion or exclusion of these cells did not alter the number or
698 identity of clusters, confirming that no biologically relevant populations were removed.

699 Count matrices were normalized such that all cells had the same total number of counts,
700 corresponding to the mean library size across the dataset. Normalized counts were log-
701 transformed using the log1p function. The resulting log-normalized matrices were used
702 for all downstream analyses, including dimensionality reduction and clustering.

703 Highly variable genes (HVGs) were identified using Scanpy's default parameters,
704 retaining the top 2,000 genes. Principal component analysis (PCA) was performed on the

705 HVG expression matrix, and the number of principal components retained was
706 determined using the elbow heuristic based on the explained variance ratio.

707 Analyses involving multiple batches or experimental conditions were batch-corrected
708 using Harmony (Korsunsky et al., 2019) applied to the PCA representation. Cell cycle
709 phase was annotated using curated gene lists (Tirosh et al., 2016), and, where necessary,
710 a second Harmony integration was performed to mitigate residual cell cycle–related
711 effects.

712 A k-nearest neighbor (KNN) graph (k = 15) was constructed from the batch- and cell-
713 cycle–corrected PCA space. Two-dimensional representations were generated using
714 UMAP for the visualization of cell population structure.

715 Clusters were identified using the Leiden algorithm (Traag et al., 2019) on the KNN graph.
716 Differential expression analysis was performed using the Wilcoxon rank-sum test with
717 Hochberg correction for multiple testing. Cluster annotation was guided by differentially
718 expressed genes and curated marker gene lists, visualized on UMAPs and summarized
719 in dot plots. P-values from differential expression analysis were interpreted as indicative
720 rather than definitive due to the inherent dependence between clustering and differential
721 expression testing.

722 Datasets were projected onto reference mouse embryo and gastruloid single-cell atlases
723 using a custom implementation of scmap (Kiselev et al., 2018). Gene identifier
724 discrepancies (e.g., Ensembl IDs vs. common gene symbols) were resolved using
725 mygene.info (Wu et al., 2013), and duplicated mappings were removed to ensure
726 consistent one-to-one correspondence prior to projection.

727 **Real-time quantitative PCR**

728 **Sample Collection and RNA Extraction**

729 The number of gastruloids harvested per time point was as follows: 48h, 96 gastruloids;
730 60h, 96 gastruloids; 72h, 72 gastruloids; 96h, 72 gastruloids; and 120h, 48 gastruloids.
731 Gastruloids were rinsed once with PBS and lysed in 350 µL of lysis buffer from the
732 HiGenoMB HiPurA Total RNA Miniprep Purification Kit (HiMedia) supplemented with
733 3.5µL of 13.4M β-mercaptoethanol. Total RNA was extracted following the manufacturer's
734 instructions. RNA yield ranged from 80 to 350ng/µL. For each sample, 1µg of total RNA
735 was reverse transcribed using the PrimeScript First Strand cDNA Synthesis Kit (Takara,
736 Cat. No. 6110A) according to the manufacturer's protocol. qPCR reactions were set up in
737 MicroAmp Optical 384-well reaction plates (Applied Biosystems, Cat. No. 4309849).
738 Reactions were prepared using Maxima SYBR Green/ROX qPCR Master Mix (Thermo
739 Fisher Scientific) and gene-specific primers. Ct values were obtained for each gene and

740 normalized to Actin (ΔCt). For temporal comparisons, relative expression for each gene
741 was normalized to the corresponding 48-h time point within each condition (ΔΔCt).

742 Statistical analyses were performed in GraphPad Prism. A two-way ordinary ANOVA was
743 performed with time as the row factor (changes in gene expression across time), condition
744 as the column factor (comparing global between PM and AM), and their interaction (to
745 determine whether temporal expression patterns differ between conditions). It was
746 followed by Sidak's post-hoc test to identify significantly different time points between
747 conditions. To evaluate changes within a condition relative to 48h, ΔCt values were
748 compared using a two-tailed paired t-test. Line graphs represent mean ± SD with data
749 points connected to illustrate temporal trends.

750 The list of primers used for RT-qPCR are provided in table 8.

751 **Methods table 8**

| Gene name | Sequence | Reference |
|---|---|---|
| *Eomes* | GACCTCCAGGGACAATCTGA | qPCR primer depot |
| | GGCCTACCAAAACACGGATA | |
| *Tbx1* | TGTGGGACGAGTTCAATCAG | (Sambasivan et al., 2009) |
| | TGTCATCTACGGGCACAAAG | |
| *Tbxt* | CATGTACTCTTTCTTGCTGG | (Lolas et al., 2014) |
| | GGTCTCGGGAAAGCAGTGGC | |
| *Wnt3* | CAAGCACAACAATGAAGCAGGC | (Hayashi et al., 2011) |
| | TCGGGACTCACGGTGTTTCTC | |
| *Wnt3a* | CTCCTCTCGGATACCTCTTAGTG | qPCR primer depot |
| | GCATGATCTCCACGTAGTTCCTG | |
| *Cdx2* | TCAACCTCGCCACAACCTTCCC | (Rayon et al., 2014) |
| | TGGCTCAGCCTGGGATTGCT | |
| *Actin* | CGCCACCAGTTCGCCATGGA | Self-generated |
| | TACAGCCCGGGGAGCATCGT | |

752 **Flow cytometry analysis**

753 Single-cell suspensions were generated from 24 120h gastruloids per condition, following
754 the dissociation protocol described in the *single-cell RNA sequencing* section. After
755 centrifugation, cell pellets were resuspended in PBS and analyzed on a Beckman Coulter
756 CytoFLEX-S flow cytometer.

757 During post-acquisition analysis, debris was excluded by gating on FSC-A versus SSC-
758 A. To define the negative population, the unlabelled E14Tg2a cell line was used as a
759 control. For the *Tcf/Lef:mCherry* and *AR8:mCherry* reporter experiments comparing PM
760 and AM gastruloids, a fluorescence threshold was set such that 95% of the negative-
761 control events fell within the negative gate. Median fluorescence intensity was then
762 calculated using only the events above this threshold.

763 For the chimeric gastruloid experiments, a single universal threshold could not be applied
764 because the samples contained mixtures of multiple cell lines, each exhibiting different
765 background fluorescence levels. As expected for chimeric samples, all conditions
766 contained both reporter-negative and reporter-positive cells, resulting in a bimodal
767 distribution of fluorescence intensities. Therefore, for each condition, the local minimum
768 between the two peaks was used as the cutoff to separate the negative and positive
769 populations. Median fluorescence intensity was subsequently calculated using only the
770 reporter-positive cells.

771 **Acknowledgements**

772 We thank Prof. Alfonso Martinez Arias and Dr. Andre Dias for their insightful discussions
773 and valuable feedback throughout this work. We are grateful to Mr. Prahlad Kashyap for
774 assistance with line-scan quantitations. We acknowledge Dr. Awadhesh Pandit, Mr.
775 Santosh Srirangam, Mr. Lakshminarayanan C.P. and Dr. H. Krishnamurthy for their
776 support with single-cell sequencing experiments. We also thank Dr. Rajesh Ladher, Dr.
777 Praveen Vemula, Dr. Dasaradhi Palakodeti and Dr. Dhandapani Perundurai for hosting
778 S.K.Y. and A.B. and facilitating the single-cell sequencing experiments in Bangalore.

779 This research was supported by the Department of Biotechnology, Government of India
780 (grants BT/PR39986/MED/97/479/2020 and BT/PR45132/MED/97/621/2022) and by
781 IISER Tirupati core funds to R.S. A.B. is supported by a UGC-JRF/SRF fellowship, S.K.Y.
782 by an IISER Tirupati Integrated PhD fellowship, and B.V. was supported by DBT-
783 JRF/SRF fellowships and an InStem fellowship.

784 **Author Contributions**

785 Conceptualization, R.S., A.B., and S.K.Y.; Methodology, A.B., S.K.Y., B.V., and R.S.;
786 Investigation, A.B., S.K.Y., and B.V.; Formal Analysis, R.S., A.B., S.K.Y., and G.T.C.;
787 Visualization, G.T.C.; Resources, B.V., A.B, S.K.Y., and R.S.; Supervision, R.S.;

788 Writing – Original Draft, R.S., A.B., and S.K.Y.; Writing – Review & Editing, R.S., A.B.,
789 and S.K.Y.

## References


Abu-Abed, S., Dollé, P., Metzger, D., Beckett, B., Chambon, P., & Petkovich, M. (2001). The retinoic acid-metabolizing enzyme, CYP26A1, is essential for normal hindbrain patterning, vertebral identity, and development of posterior structures. *Genes & Development*, *15*(2), 226. https://doi.org/10.1101/GAD.855001

Amblard, I., Baranasic, D., Xie, S. Q., Moyon, B., Percharde, M., Lenhard, B., & Metzis, V. (2025). A dual enhancer-attenuator element ensures transient Cdx2 expression during mouse posterior body formation. *Developmental Cell*, *60*(18). https://doi.org/10.1016/j.devcel.2025.06.006

Amin, S., Neijts, R., Simmini, S., Van Rooijen, C., Tan, S. C., Kester, L., Van Oudenaarden, A., Creyghton, M. P., & Deschamps, J. (2016). Cdx and T Brachyury Co-activate Growth Signaling in the Embryonic Axial Progenitor Niche. *Cell Reports*, *17*(12), 3165–3177. https://doi.org/10.1016/j.celrep.2016.11.069

Ang, H. L., Deltour, L., Hayamizu, T. F., Žgombić-Knight, M., & Duester, G. (1996). Retinoic acid synthesis in mouse embryos during gastrulation and craniofacial development linked to class IV alcohol dehydrogenase gene expression. *Journal of Biological Chemistry*, *271*(16), 9526–9534. https://doi.org/10.1074/JBC.271.16.9526

Arnold, S. J., Hofmann, U. K., Bikoff, E. K., & Robertson, E. J. (2008). Pivotal roles for eomesodermin during axis formation,epithelium-to-mesenchyme transition and endoderm specification in the mouse. *Development*, *135*(3), 501–511. https://doi.org/10.1242/dev.014357

Arnold, S. J., & Robertson, E. J. (2009). Making a commitment: cell lineage allocation and axis patterning in the early mouse embryo. *Nature Reviews Molecular Cell Biology 2009 10:2*, *10*(2), 91–103. https://doi.org/10.1038/nrm2618

Beccari, L., Moris, N., Girgin, M., Turner, D. A., Baillie-Johnson, P., Cossy, A. C., Lutolf, M. P., Duboule, D., & Arias, A. M. (2018). Multi-axial self-organization properties of mouse embryonic stem cells into gastruloids. *Nature 2018 562:7726*, *562*(7726), 272–276. https://doi.org/10.1038/s41586-018-0578-0

Cañestro, C., Postlethwait, J. H., Gonzàlez-Duarte, R., & Albalat, R. (2006). Is retinoic acid genetic machinery a chordate innovation? *Evolution and Development*, *8*(5), 394–406. https://doi.org/10.1111/J.1525-142X.2006.00113.X

Chapman, D. L., & Papaioannou, V. E. (1998). Three neural tubes in mouse embryos with mutations in the T-box gene Tbx6. *Nature 1998 391:6668*, *391*(6668), 695–697. https://doi.org/10.1038/35624

Chawengsaksophak, K., De Graaff, W., Rossant, J., Deschamps, J., & Beck, F. (2004). Cdx2 is essential for axial elongation in mouse development. *Proceedings of the National Academy of Sciences of the United States of America*, *101*(20), 7641–7645. https://doi.org/10.1073/PNAS.0401654101;PAGEGROUP:STRING:PUBLICATION

Ciruna, B., & Rossant, J. (2001). FGF Signaling Regulates Mesoderm Cell Fate Specification and Morphogenetic Movement at the Primitive Streak. *Developmental Cell*, *1*(1), 37–49. https://doi.org/10.1016/S1534-5807(01)00017-X

Costello, I., Pimeisl, I. M., Dräger, S., Bikoff, E. K., Robertson, E. J., & Arnold, S. J. (2011). The T-box transcription factor Eomesodermin acts upstream of Mesp1 to specify cardiac

833 mesoderm during mouse gastrulation. *Nature Cell Biology 2011 13:9*, *13*(9), 1084–1091.
834 https://doi.org/10.1038/ncb2304
835 Deschamps, J., & van Nes, J. (2005). Developmental regulation of the Hox genes during axial
836 morphogenesis in the mouse. *Development*, *132*(13), 2931–2942.
837 https://doi.org/10.1242/DEV.01897
838 Dias, A., Pascual-Mas, P., Robertson, G., Torregrosa-Cortés, G., Stelloo, S., Casaní-Galdón, P.,
839 Babin, S., Romaniuk, Y., Mayran, A., Wehmeyer, A. E., Garcia-Ojalvo, J., McNamara, H. M.,
840 Vermeulen, M., Arnold, S. J., & Arias, A. M. (2025). Opposing Nodal and Wnt signalling
841 activities govern the emergence of the mammalian body plan. *BioRxiv*, 2025.01.11.632562.
842 https://doi.org/10.1101/2025.01.11.632562
843 Doetschman, T., Gregg, R. G., Maeda, N., Hooper, M. L., Melton, D. W., Thompson, S., &
844 Smithies, O. (1987). Targetted correction of a mutant HPRT gene in mouse embryonic stem
845 cells. *Nature*, *330*(6148), 576–578. https://doi.org/10.1038/330576A0;KWRD
846 Durston, A. J., Timmermans, J. P. M., Hage, W. J., Hendriks, H. F. J., De Vries, N. J., Heideveld,
847 M., & Nieuwkoop, P. D. (1989). Retinoic acid causes an anteroposterior transformation in
848 the developing central nervous system. *Nature 1989 340:6229*, *340*(6229), 140–144.
849 https://doi.org/10.1038/340140a0
850 Ee, L. sha, Medina-Cano, D., Goetzler, E., Uyehara, C., Schwarz, C., Salataj, E., Madhuranath,
851 S., Evans, T., Hadjantonakis, A. K., Apostolou, E., Polyzos, A., Vierbuchen, T., & Stadtfeld,
852 M. (2025). Enhancer remodeling by OTX2 directs specification and patterning of mammalian
853 definitive endoderm. *Developmental Cell*, *0*(0). https://doi.org/10.1016/j.devcel.2025.07.020
854 Evans, A. L., Faial, T., Gilchrist, M. J., Down, T., Vallier, L., Pedersen, R. A., Wardle, F. C., &
855 Smith, J. C. (2012). Genomic targets of Brachyury (T) in differentiating mouse embryonic
856 stem cells. *PloS One*, *7*(3). https://doi.org/10.1371/JOURNAL.PONE.0033346
857 Faunes, F., Hayward, P., Descalzo, S. M., Chatterjee, S. S., Balayo, T., Trott, J., Christoforou, A.,
858 Ferrer-Vaquer, A., Hadjantonakis, A. K., Dasgupta, R., & Arias, A. M. (2013). A membrane-
859 associated β-catenin/Oct4 complex correlates with ground-state pluripotency in mouse
860 embryonic stem cells. *Development (Cambridge)*, *140*(6), 1171–1183.
861 https://doi.org/10.1242/DEV.085654/VIDEO-3
862 Ferrer-Vaquer, A., Piliszek, A., Tian, G., Aho, R. J., Dufort, D., & Hadjantonakis, A. K. (2010). A
863 sensitive and bright single-cell resolution live imaging reporter of Wnt/ß-catenin signaling in
864 the mouse. *BMC Developmental Biology 2010 10:1*, *10*(1), 121-.
865 https://doi.org/10.1186/1471-213X-10-121
866 Gouti, M., Tsakiridis, A., Wymeersch, F. J., Huang, Y., Kleinjung, J., Wilson, V., & Briscoe, J.
867 (2014). In Vitro Generation of Neuromesodermal Progenitors Reveals Distinct Roles for Wnt
868 Signalling in the Specification of Spinal Cord and Paraxial Mesoderm Identity. *PLOS Biology*,
869 *12*(8), e1001937. https://doi.org/10.1371/JOURNAL.PBIO.1001937
870 Hayashi, K., Ohta, H., Kurimoto, K., Aramaki, S., & Saitou, M. (2011). Reconstitution of the mouse
871 germ cell specification pathway in culture by pluripotent stem cells. *Cell*, *146*(4), 519–532.
872 https://doi.org/10.1016/j.cell.2011.06.052
873 Hennessy, M. J., Fulton, T., Turner, D. A., & Steventon, B. (2023). Negative feedback on Retinoic
874 Acid by Brachyury guides gastruloid symmetry-breaking. *BioRxiv*, 2023.06.02.543388.
875 https://doi.org/10.1101/2023.06.02.543388

Herrmann, B. G. (1991). Expression pattern of the Brachyury gene in whole-mount TWIS/TWIS mutant embryos. *Development*, *113*(3), 913–917. https://doi.org/10.1242/DEV.113.3.913

Hikasa, H., & Sokol, S. Y. (2013). Wnt Signaling in Vertebrate Axis Specification. *Cold Spring Harbor Perspectives in Biology*, *5*(1), a007955. https://doi.org/10.1101/CSHPERSPECT.A007955

Ikeya, M., & Takada, S. (2001). Wnt-3a is required for somite specification along the anteroposterior axis of the mouse embryo and for regulation of cdx-1 expression. *Mechanisms of Development*, *103*(1–2), 27–33. https://doi.org/10.1016/s0925-4773(01)00338-0

Iulianella, A., Beckett, B., Petkovich, M., & Lohnes, D. (1999). A Molecular Basis for Retinoic Acid-Induced Axial Truncation. *Developmental Biology*, *205*(1), 33–48. https://doi.org/10.1006/DBIO.1998.9110

Javali, A., Misra, A., Leonavicius, K., Acharyya, D., Vyas, B., & Sambasivan, R. (2017). Co-expression of Tbx6 and Sox2 identifies a novel transient neuromesoderm progenitor cell state. *Development (Cambridge)*, *144*(24), 4522–4529. https://doi.org/10.1242/DEV.153262/264518/AM/CO-EXPRESSION-OF-TBX6-AND-SOX2-IDENTIFIES-A-NOVEL

Jho, E., Zhang, T., Domon, C., Joo, C.-K., Freund, J.-N., & Costantini, F. (2002). Wnt/β-Catenin/Tcf Signaling Induces the Transcription of Axin2, a Negative Regulator of the Signaling Pathway. *Molecular and Cellular Biology*, *22*(4), 1172–1183. https://doi.org/10.1128/MCB.22.4.1172-1183.2002;PAGE:STRING:ARTICLE/CHAPTER

Kessel, M. (1992). Respecification of vertebral identities by retinoic acid. *Development*, *115*(2), 487–501. https://doi.org/10.1242/DEV.115.2.487

Kessel, M., & Gruss, P. (1991). Homeotic transformations of murine vertebrae and concomitant alteration of Hox codes induced by retinoic acid. *Cell*, *67*(1), 89–104. https://doi.org/10.1016/0092-8674(91)90574-I

Kinder, S. J., Hadjantonakis, A.-K., Quinlan, G. A., Tam, P. P. L., Nagy, A., & Tsang, T. E. (1999). The orderly allocation of mesodermal cells to the extraembryonic structures and the anteroposterior axis during gastrulation of the mouse embryo. *Development*, *126*(21), 4691–4701. https://doi.org/10.1242/dev.126.21.4691

Kiselev, V. Y., Yiu, A., & Hemberg, M. (2018). scmap: projection of single-cell RNA-seq data across data sets. *Nature Methods 2018 15:5*, *15*(5), 359–362. https://doi.org/10.1038/nmeth.4644

Korsunsky, I., Millard, N., Fan, J., Slowikowski, K., Zhang, F., Wei, K., Baglaenko, Y., Brenner, M., Loh, P. ru, & Raychaudhuri, S. (2019). Fast, sensitive and accurate integration of single-cell data with Harmony. *Nature Methods 2019 16:12*, *16*(12), 1289–1296. https://doi.org/10.1038/s41592-019-0619-0

Langston, A. W., & Gudas, L. J. (1994). Retinoic acid and homeobox gene regulation. *Current Opinion in Genetics & Development*, *4*(4), 550–555. https://doi.org/10.1016/0959-437X(94)90071-A

Lawson, K. A., Meneses, J. J., & Pedersen, R. A. (1991). Clonal analysis of epiblast fate during germ layer formation in the mouse embryo. *Development*, *113*(3), 891–911. https://doi.org/10.1242/dev.113.3.891

Lickert, H., Huls, G., Clevers, H., Kemler, R., Domon, C., Duluc, I., Freund, J.-N., Meyer, B. I., & Wehrle, C. (2000). Wnt/(beta)-catenin signaling regulates the expression of the homeobox gene Cdx1 in embryonic intestine. *Development*, *127*(17), 3805–3813. https://doi.org/10.1242/dev.127.17.3805

Lolas, M., Valenzuela, P. D. T., Tjian, R., & Liu, Z. (2014). Charting Brachyury-mediated developmental pathways during early mouse embryogenesis. *Proceedings of the National Academy of Sciences of the United States of America*, *111*(12), 4478–4483. https://doi.org/10.1073/PNAS.1402612111;WEBSITE:WEBSITE:PNAS-SITE;ISSUE:ISSUE:DOI

Marlétaz, F., Holland, L. Z., Laudet, V., & Schubert, M. (2006). Retinoic acid signaling and the evolution of chordates. *International Journal of Biological Sciences*, *2*(2), 38. https://doi.org/10.7150/IJBS.2.38

Martin, B. L., & Kimelman, D. (2008). Regulation of Canonical Wnt Signaling by Brachyury Is Essential for Posterior Mesoderm Formation. *Developmental Cell*, *15*(1), 121–133. https://doi.org/10.1016/j.devcel.2008.04.013

Martin, B. L., & Kimelman, D. (2009). Wnt Signaling and the Evolution of Embryonic Posterior Development. *Current Biology*, *19*(5), R215–R219. https://doi.org/10.1016/j.cub.2009.01.052

Martinez-Barbera, J. P., Rodriguez, T. A., & Beddington, R. S. P. (2000). The Homeobox Gene Hesx1 Is Required in the Anterior Neural Ectoderm for Normal Forebrain Formation. *Developmental Biology*, *223*(2), 422–430. https://doi.org/10.1006/DBIO.2000.9757

Mayran, A., Kolly, D., Lopez-Delisle, L., Romaniuk, Y., Leonardi, M., Cossy, A.-C., Lacroix, T., Rekaik, H., Amândio, A. R., Osteil, P., & Duboule, D. (2025). Cadherins modulate the self-organizing potential of pseudo-embryos. *Cell Reports*, *44*(11), 116567. https://doi.org/10.1016/j.celrep.2025.116567

McNamara, H. M., Solley, S. C., Adamson, B., Chan, M. M., & Toettcher, J. E. (2024). Recording morphogen signals reveals mechanisms underlying gastruloid symmetry breaking. *Nature Cell Biology 2024 26:11*, *26*(11), 1832–1844. https://doi.org/10.1038/s41556-024-01521-9

Moore-Scott, B. A., & Manley, N. R. (2005). Differential expression of Sonic hedgehog along the anterior-posterior axis regulates patterning of pharyngeal pouch endoderm and pharyngeal endoderm-derived organs. *Developmental Biology*, *278*(2), 323–335. https://doi.org/10.1016/J.YDBIO.2004.10.027

Nandkishore, N., Vyas, B., Javali, A., Ghosh, S., & Sambasivan, R. (2018). Divergent early mesoderm specification underlies distinct head and trunk muscle programmes in vertebrates. *Development (Cambridge)*, *145*(18), 173187. https://doi.org/10.1242/DEV.160945/48477

Neijts, R., Amin, S., van Rooijen, C., & Deschamps, J. (2017). Cdx is crucial for the timing mechanism driving colinear Hox activation and defines a trunk segment in the Hox cluster topology. *Developmental Biology*, *422*(2), 146–154. https://doi.org/10.1016/J.YDBIO.2016.12.024

Neijts, R., Simmini, S., Giuliani, F., van Rooijen, C., & Deschamps, J. (2014). Region-specific regulation of posterior axial elongation during vertebrate embryogenesis. *Developmental Dynamics*, *243*(1), 88–98. https://doi.org/10.1002/DVDY.24027;ISSUE:ISSUE:DOI

Niederreither, K., Subbarayan, V., Dollé, P., & Chambon, P. (1999). Embryonic retinoic acid synthesis is essential for early mouse post-implantation development. *Nature Genetics 1999 21:4*, *21*(4), 444–448. https://doi.org/10.1038/7788

Niehrs, C., Kazanskaya, O., Wu, W., & Glinka, A. (2001). Dickkopf1 and the Spemann-Mangold head organizer. In *Int. J. Dev. Biol* (Vol. 45). www.ijdb.ehu.es

Nolte, C., De Kumar, B., & Krumlauf, R. (2019). Hox genes: Downstream "effectors" of retinoic acid signaling in vertebrate embryogenesis. *Genesis*, *57*(7), e23306. https://doi.org/10.1002/DVG.23306;ISSUE:ISSUE:DOI

Nowotschin, S., Ferrer-Vaquer, A., Concepcion, D., Papaioannou, V. E., & Hadjantonakis, A. K. (2012). Interaction of Wnt3a, Msgn1 and Tbx6 in neural versus paraxial mesoderm lineage commitment and paraxial mesoderm differentiation in the mouse embryo. *Developmental Biology*, *367*(1), 1–14. https://doi.org/10.1016/J.YDBIO.2012.04.012

Pijuan-Sala, B., Griffiths, J. A., Guibentif, C., Hiscock, T. W., Jawaid, W., Calero-Nieto, F. J., Mulas, C., Ibarra-Soria, X., Tyser, R. C. V., Ho, D. L. L., Reik, W., Srinivas, S., Simons, B. D., Nichols, J., Marioni, J. C., & Göttgens, B. (2019). A single-cell molecular map of mouse gastrulation and early organogenesis. *Nature 2019 566:7745*, *566*(7745), 490–495. https://doi.org/10.1038/s41586-019-0933-9

Pilon, N., Oh, K., Sylvestre, J. R., Bouchard, N., Savory, J., & Lohnes, D. (2006). Cdx4 is a direct target of the canonical Wnt pathway. *Developmental Biology*, *289*(1), 55–63. https://doi.org/10.1016/J.YDBIO.2005.10.005

Pilon, N., Oh, K., Sylvestre, J. R., Savory, J. G. A., & Lohnes, D. (2007). Wnt signaling is a key mediator of Cdx1 expression in vivo. *Development (Cambridge, England)*, *134*(12), 2315–2323. https://doi.org/10.1242/DEV.001206

Ramkumar, N., & Anderson, K. V. (2011). SnapShot: Mouse Primitive Streak. *Cell*, *146*(3), 488-488.e2. https://doi.org/10.1016/J.CELL.2011.07.028

Rawat, V. P. S., Thoene, S., Naidu, V. M., Arseni, N., Heilmeier, B., Metzeler, K., Petropoulos, K., Deshpande, A., Quintanilla-Martinez, L., Bohlander, S. K., Spiekermann, K., Hiddemann, W., Feuring-Buske, M., & Buske, C. (2008). Overexpression of CDX2 perturbs HOX gene expression in murine progenitors depending on its N-terminal domain and is closely correlated with deregulated HOX gene expression in human acute myeloid leukemia. *Blood*, *111*(1), 309–319. https://doi.org/10.1182/BLOOD-2007-04-085407

Rayon, T., Menchero, S., Nieto, A., Xenopoulos, P., Crespo, M., Cockburn, K., Cañon, S., Sasaki, H., Hadjantonakis, A. K., de la Pompa, J. L., Rossant, J., & Manzanares, M. (2014). Notch and Hippo Converge on Cdx2 to Specify the Trophectoderm Lineage in the Mouse Blastocyst. *Developmental Cell*, *30*(4), 410–422. https://doi.org/10.1016/j.devcel.2014.06.019

Rekaik, H., Lopez-Delisle, L., Hintermann, A., Mascrez, B., Bochaton, C., Mayran, A., & Duboule, D. (2023). Sequential and directional insulation by conserved CTCF sites underlies the Hox timer in stembryos. *Nature Genetics 2023 55:7*, *55*(7), 1164–1175. https://doi.org/10.1038/s41588-023-01426-7

Rhinn, M., & Dollé, P. (2012). Retinoic acid signalling during development. *Development (Cambridge, England)*, *139*(5), 843–858. https://doi.org/10.1242/DEV.065938

1004 Robertson, E. J. (2014). Dose-dependent Nodal/Smad signals pattern the early mouse embryo.
1005 *Seminars in Cell & Developmental Biology*, *32*, 73–79.
1006 https://doi.org/10.1016/J.SEMCDB.2014.03.028
1007 Rosen, L. U., Stapel, L. C., Argelaguet, R., Barker, C. G., Yang, A., Reik, W., & Marioni, J. C.
1008 (2022). Inter-gastruloid heterogeneity revealed by single cell transcriptomics time course:
1009 implications for organoid based perturbation studies. *BioRxiv*, 2022.09.27.509783.
1010 https://doi.org/10.1101/2022.09.27.509783
1011 Rossant, J., Zirngibl, R., Cado, D., Shago, M., & Giguère, V. (1991). Expression of a retinoic acid
1012 response element-hsplacZ transgene defines specific domains of transcriptional activity
1013 during mouse embryogenesis. *Genes & Development*, *5*(8), 1333–1344.
1014 https://doi.org/10.1101/GAD.5.8.1333
1015 Rossi, G., Broguiere, N., Miyamoto, M., Boni, A., Guiet, R., Girgin, M., Kelly, R. G., Kwon, C., &
1016 Lutolf, M. P. (2021). Capturing Cardiogenesis in Gastruloids. *Cell Stem Cell*, *28*(2), 230-
1017 240.e6. https://doi.org/10.1016/j.stem.2020.10.013
1018 Ruiz I Altaba, A., & Jessell, T. (1991). Retinoic acid modifies mesodermal patterning in early
1019 Xenopus embryos. *Genes & Development*, *5*(2), 175–187.
1020 https://doi.org/10.1101/GAD.5.2.175
1021 Ruiz I Altaba, S., & Jessell, T. M. (1991). Retinoic acid modifies the pattern of cell differentiation
1022 in the central nervous system of neurula stage Xenopus embryos. *Development*, *112*(4),
1023 945–958. https://doi.org/10.1242/DEV.112.4.945
1024 Russ, A. P., Wattler, S., Colledge, W. H., Aparicio, S. A. J. R., Carlton, M. B. L., Pearce, J. J.,
1025 Barton, S. C., Azim Surani, M., Ryan, K., Nehls, M. C., Wilsons, V., & Evans, M. J. (2000).
1026 Eomesodermin is required for mouse trophoblast development and mesoderm formation.
1027 *Nature 2000 404:6773*, *404*(6773), 95–99. https://doi.org/10.1038/35003601
1028 Sambasivan, R., Gayraud-Morel, B., Dumas, G., Cimper, C., Paisant, S., Kelly, R., & Tajbakhsh,
1029 S. (2009). Distinct Regulatory Cascades Govern Extraocular and Pharyngeal Arch Muscle
1030 Progenitor Cell Fates. *Developmental Cell*, *16*(6), 810–821.
1031 https://doi.org/10.1016/j.devcel.2009.05.008
1032 Sambasivan, R., & Steventon, B. (2021). Neuromesodermal Progenitors: A Basis for Robust Axial
1033 Patterning in Development and Evolution. *Frontiers in Cell and Developmental Biology*, *8*,
1034 607516. https://doi.org/10.3389/FCELL.2020.607516/BIBTEX
1035 Schubert, M., Holland, N. D., Laudet, V., & Holland, L. Z. (2006). A retinoic acid-Hox hierarchy
1036 controls both anterior/posterior patterning and neuronal specification in the developing
1037 central nervous system of the cephalochordate amphioxus. *Developmental Biology*, *296*(1),
1038 190–202. https://doi.org/10.1016/J.YDBIO.2006.04.457
1039 Schüle, K. M., Weckerle, J., Probst, S., Wehmeyer, A. E., Zissel, L., Schröder, C. M., Tekman,
1040 M., Kim, G. J., Schlägl, I. M., Sagar, & Arnold, S. J. (2023). Eomes restricts Brachyury
1041 functions at the onset of mouse gastrulation. *Developmental Cell*, *58*(18), 1627-1642.e7.
1042 https://doi.org/10.1016/j.devcel.2023.07.023
1043 Schwaiger, M., Andrikou, C., Dnyansagar, R., Murguia, P. F., Paganos, P., Voronov, D.,
1044 Zimmermann, B., Lebedeva, T., Schmidt, H. A., Genikhovich, G., Benvenuto, G., Arnone, M.
1045 I., & Technau, U. (2022). An ancestral Wnt-Brachyury feedback loop in axial patterning and
1046 recruitment of mesoderm-determining target genes. *Nature Ecology & Evolution*, *6*(12),
1047 1921–1939. https://doi.org/10.1038/S41559-022-01905-W

1048 Serup, P., Gustavsen, C., Klein, T., Potter, L. A., Lin, R., Mullapudi, N., Wandzioch, E., Hines, A.,
1049 Davis, A., Bruun, C., Engberg, N., Petersen, D. R., Peterslund, J. M. L., MacDonald, R. J.,
1050 Grapin-Botton, A., Magnuson, M. A., & Zaret, K. S. (2012). Partial promoter substitutions
1051 generating transcriptional sentinels of diverse signaling pathways in embryonic stem cells
1052 and mice. *DMM Disease Models and Mechanisms*, *5*(6), 956–966.
1053 https://doi.org/10.1242/DMM.009696/258717/AM/PARTIAL-PROMOTER-
1054 SUBSTITUTIONS-GENERATING
1055 Simeone, A., & Acampora, D. (2001). Otx2 function in murine gastrulation The role of Otx2 in
1056 organizing the anterior patterning in mouse. In *Int. J. Dev. Biol* (Vol. 45). www.ijdb.ehu.es
1057 Simon, C. S., Downes, D. J., Gosden, M. E., Telenius, J., Higgs, D. R., Hughes, J. R., Costello,
1058 I., Bikoff, E. K., & Robertson, E. J. (2017). Functional characterisation of cis-regulatory
1059 elements governing dynamic Eomes expression in the early mouse embryo. *Development*
1060 *(Cambridge)*, *144*(7), 1249–1260.
1061 https://doi.org/10.1242/DEV.147322/264330/AM/FUNCTIONAL-CHARACTERISATION-
1062 OF-CIS-REGULATORY
1063 Smith, J. C., Price, B. M. J., Green, J. B. A., Weigel, D., & Herrmann, B. G. (1991). Expression of
1064 a xenopus homolog of Brachyury (T) is an immediate-early response to mesoderm induction.
1065 *Cell*, *67*(1), 79–87. https://doi.org/10.1016/0092-8674(91)90573-H
1066 Stern, C. D., Charité, J., Deschamps, J., Duboule, D., Durston, A. J., Kmita, M., Nicolas, J.-F.,
1067 Palmeirim, I., Smith, J. C., & Wolpert, L. (2006). Head-tail patterning of the vertebrate
1068 embryo: one, two or many unresolved problems? *The International Journal of Developmental*
1069 *Biology*, *50*(1), 3–15. https://doi.org/10.1387/ijdb.052095cs
1070 Suppinger, S., Zinner, M., Aizarani, N., Lukonin, I., Ortiz, R., Azzi, C., Stadler, M. B., Vianello, S.,
1071 Palla, G., Kohler, H., Mayran, A., Lutolf, M. P., & Liberali, P. (2023). Multimodal
1072 characterization of murine gastruloid development. *Cell Stem Cell*, *30*(6), 867-884.e11.
1073 https://doi.org/10.1016/J.STEM.2023.04.018
1074 Sussel, L., Marin, O., Kimura, S., & Rubenstein, J. L. R. (1999). Loss of Nkx2.1 homeobox gene
1075 function results in a ventral to dorsal molecular respecification within the basal
1076 telencephalon: evidence for a transformation of the pallidum into the striatum. *Development*,
1077 *126*(15), 3359–3370. https://doi.org/10.1242/DEV.126.15.3359
1078 Takada, S., Stark, K. L., Shea, M. J., Vassileva, G., McMahon, J. A., & McMahon, A. P. (1994).
1079 Wnt-3a regulates somite and tailbud formation in the mouse embryo. *Genes & Development*,
1080 *8*(2), 174–189. https://doi.org/10.1101/GAD.8.2.174
1081 Takemoto, T., Uchikawa, M., Yoshida, M., Bell, D. M., Lovell-Badge, R., Papaioannou, V. E., &
1082 Kondoh, H. (2011). Tbx6-dependent Sox2 regulation determines neural or mesodermal fate
1083 in axial stem cells. *Nature 2011 470:7334*, *470*(7334), 394–398.
1084 https://doi.org/10.1038/nature09729
1085 Thomas, P., & Beddington, R. (1996). Anterior primitive endoderm may be responsible for
1086 patterning the anterior neural plate in the mouse embryo. *Current Biology*, *6*(11), 1487–1496.
1087 https://doi.org/10.1016/S0960-9822(96)00753-1
1088 Thomas, P. Q., Dattani, M. T., Brickman, J. M., McNay, D., Warne, G., Zacharin, M., Cameron,
1089 F., Hurst, J., Woods, K., Dunger, D., Stanhope, R., Forrest, S., Robinson, I. C. A. F., &
1090 Beddington, R. S. P. (2001). Heterozygous HESX1 mutations associated with isolated

congenital pituitary hypoplasia and septo-optic dysplasia. *Human Molecular Genetics*, *10*(1), 39–45. https://doi.org/10.1093/HMG/10.1.39

Tian, T., & Meng, A. M. (2006). Nodal signals pattern vertebrate embryos. *Cellular and Molecular Life Sciences*, *63*(6), 672–685. https://doi.org/10.1007/S00018-005-5503-7/METRICS

Tirosh, I., Izar, B., Prakadan, S. M., Wadsworth, M. H., Treacy, D., Trombetta, J. J., Rotem, A., Rodman, C., Lian, C., Murphy, G., Fallahi-Sichani, M., Dutton-Regester, K., Lin, J. R., Cohen, O., Shah, P., Lu, D., Genshaft, A. S., Hughes, T. K., Ziegler, C. G. K., … Garraway, L. A. (2016). Dissecting the multicellular ecosystem of metastatic melanoma by single-cell RNA-seq. *Science*, *352*(6282), 189–196. https://doi.org/10.1126/SCIENCE.AAD0501;JOURNAL:JOURNAL:SCIENCE;WGROUP:STRING:PUBLICATION

Traag, V. A., Waltman, L., & van Eck, N. J. (2019). From Louvain to Leiden: guaranteeing well-connected communities. *Scientific Reports*, *9*(1). https://doi.org/10.1038/S41598-019-41695-Z

Turner, D. A., Girgin, M., Alonso-Crisostomo, L., Trivedi, V., Baillie-Johnson, P., Glodowski, C. R., Hayward, P. C., Collignon, J., Gustavsen, C., Serup, P., Steventon, B., Lutolf, M. P., & Arias, A. M. (2017). Anteroposterior polarity and elongation in the absence of extraembryonic tissues and of spatially localised signalling in gastruloids: Mammalian embryonic organoids. *Development (Cambridge)*, *144*(21), 3894–3906. https://doi.org/10.1242/DEV.150391/VIDEO-2

Turner, D. A., Rué, P., Mackenzie, J. P., Davies, E., & Martinez Arias, A. (2014). Brachyury cooperates with Wnt/β-catenin signalling to elicit primitive-streak-like behaviour in differentiating mouse embryonic stem cells. *BMC Biology 2014 12:1*, *12*(1), 63-. https://doi.org/10.1186/S12915-014-0063-7

Uehara, M., Yashiro, K., Takaoka, K., Yamamoto, M., & Hamada, H. (2009). Removal of maternal retinoic acid by embryonic CYP26 is required for correct Nodal expression during early embryonic patterning. *Genes & Development*, *23*(14), 1689–1698. https://doi.org/10.1101/GAD.1776209

van de Ven, C., Bialecka, M., Neijts, R., Young, T., Rowland, J. E., Stringer, E. J., van Rooijen, C., Meijlink, F., Nóvoa, A., Freund, J. N., Mallo, M., Beck, F., & Deschamps, J. (2011). Concerted involvement of Cdx/Hox genes and Wnt signaling in morphogenesis of the caudal neural tube and cloacal derivatives from the posterior growth zone. *Development*, *138*(16), 3451–3462. https://doi.org/10.1242/DEV.066118

van den Akker, E., Forlani, S., Chawengsaksophak, K., de Graaft, W., Beck, F., Meyer, B. I., & Deschamps, J. (2002). Cdx1 and Cdx2 have overlapping functions in anteroposterior patterning and posterior axis elongation. *Development*, *129*(9), 2181–2193. https://doi.org/10.1242/DEV.129.9.2181

Van Den Ameele, J., Tiberi, L., Bondue, A., Paulissen, C., Herpoel, A., Iacovino, M., Kyba, M., Blanpain, C., & Vanderhaeghen, P. (2012). Eomesodermin induces Mesp1 expression and cardiac differentiation from embryonic stem cells in the absence of Activin. *EMBO Reports*, *13*(4), 355–362. https://doi.org/10.1038/EMBOR.2012.23/FIGURES/4

van den Brink, S. C., Alemany, A., van Batenburg, V., Moris, N., Blotenburg, M., Vivié, J., Baillie-Johnson, P., Nichols, J., Sonnen, K. F., Martinez Arias, A., & van Oudenaarden, A. (2020).

Single-cell and spatial transcriptomics reveal somitogenesis in gastruloids. *Nature 2020 582:7812*, *582*(7812), 405–409. https://doi.org/10.1038/s41586-020-2024-3

van Rooijen, C., Simmini, S., Bialecka, M., Neijts, R., van de Ven, C., Beck, F., & Deschamps, J. (2012). Evolutionarily conserved requirement of Cdx for post-occipital tissue emergence. *Development*, *139*(14), 2576–2583. https://doi.org/10.1242/DEV.079848

Vyas, B., Nandkishore, N., & Sambasivan, R. (2019). Vertebrate cranial mesoderm: developmental trajectory and evolutionary origin. *Cellular and Molecular Life Sciences 2019 77:10*, *77*(10), 1933–1945. https://doi.org/10.1007/S00018-019-03373-1

Wang, W. C. H., & Shashikant, C. S. (2007). Evidence for positive and negative regulation of the mouse Cdx2 gene. *Journal of Experimental Zoology Part B: Molecular and Developmental Evolution*, *308B*(3), 308–321. https://doi.org/10.1002/JEZ.B.21154

Wehmeyer, A. E., Schmitt, J. K., Eggersdorfer, F., Zissel, L., Schröder, C. M., Tekman, M., Dias, A., Schüle, K. M., Probst, S., Martinez-Arias, A., McDole, K., & Arnold, S. J. (2025). Competing regulatory modules control the transition between mammalian gastrulation modes. *BioRxiv*, 2025.05.07.652670. https://doi.org/10.1101/2025.05.07.652670

Wolf, F. A., Angerer, P., & Theis, F. J. (2018). SCANPY: large-scale single-cell gene expression data analysis. *Genome Biology 2018 19:1*, *19*(1), 15-. https://doi.org/10.1186/S13059-017-1382-0

Wolock, S. L., Lopez, R., & Klein, A. M. (2019). Scrublet: Computational Identification of Cell Doublets in Single-Cell Transcriptomic Data. *Cell Systems*, *8*(4), 281-291.e9. https://doi.org/10.1016/j.cels.2018.11.005

Wu, C., MacLeod, I., & Su, A. I. (2013). BioGPS and MyGene.info: organizing online, gene-centric information. *Nucleic Acids Research*, *41*(D1), D561–D565. https://doi.org/10.1093/NAR/GKS1114

Yamaguchi, T. P. (2001). Heads or tails: Wnts and anterior-posterior patterning. *Current Biology*, *11*(17), R713–R724. https://doi.org/10.1016/S0960-9822(01)00417-1

Yamaguchi, T. P., Yoshikawa, Y., Wu, N., Mcmahon, A. P., & Takada, S. (1999). T (Brachyury) is a direct target of Wnt3a during paraxial mesoderm specification. *Genes & Development*, *13*(24), 3185–3190. https://doi.org/10.1101/gad.13.24.3185

Young, T., & Deschamps, J. (2009). Chapter 8 Hox, Cdx, and Anteroposterior Patterning in the Mouse Embryo. *Current Topics in Developmental Biology*, *88*, 235–255. https://doi.org/10.1016/S0070-2153(09)88008-3

Young, T., Rowland, J. E., van de Ven, C., Bialecka, M., Novoa, A., Carapuco, M., van Nes, J., de Graaff, W., Duluc, I., Freund, J. N., Beck, F., Mallo, M., & Deschamps, J. (2009). Cdx and Hox Genes Differentially Regulate Posterior Axial Growth in Mammalian Embryos. *Developmental Cell*, *17*(4), 516–526. https://doi.org/10.1016/j.devcel.2009.08.010

Zou, D., Silvius, D., Davenport, J., Grifone, R., Maire, P., & Xu, P. X. (2006). Patterning of the third pharyngeal pouch into thymus/parathyroid by Six and Eya1. *Developmental Biology*, *293*(2), 499–512. https://doi.org/10.1016/J.YDBIO.2005.12.015

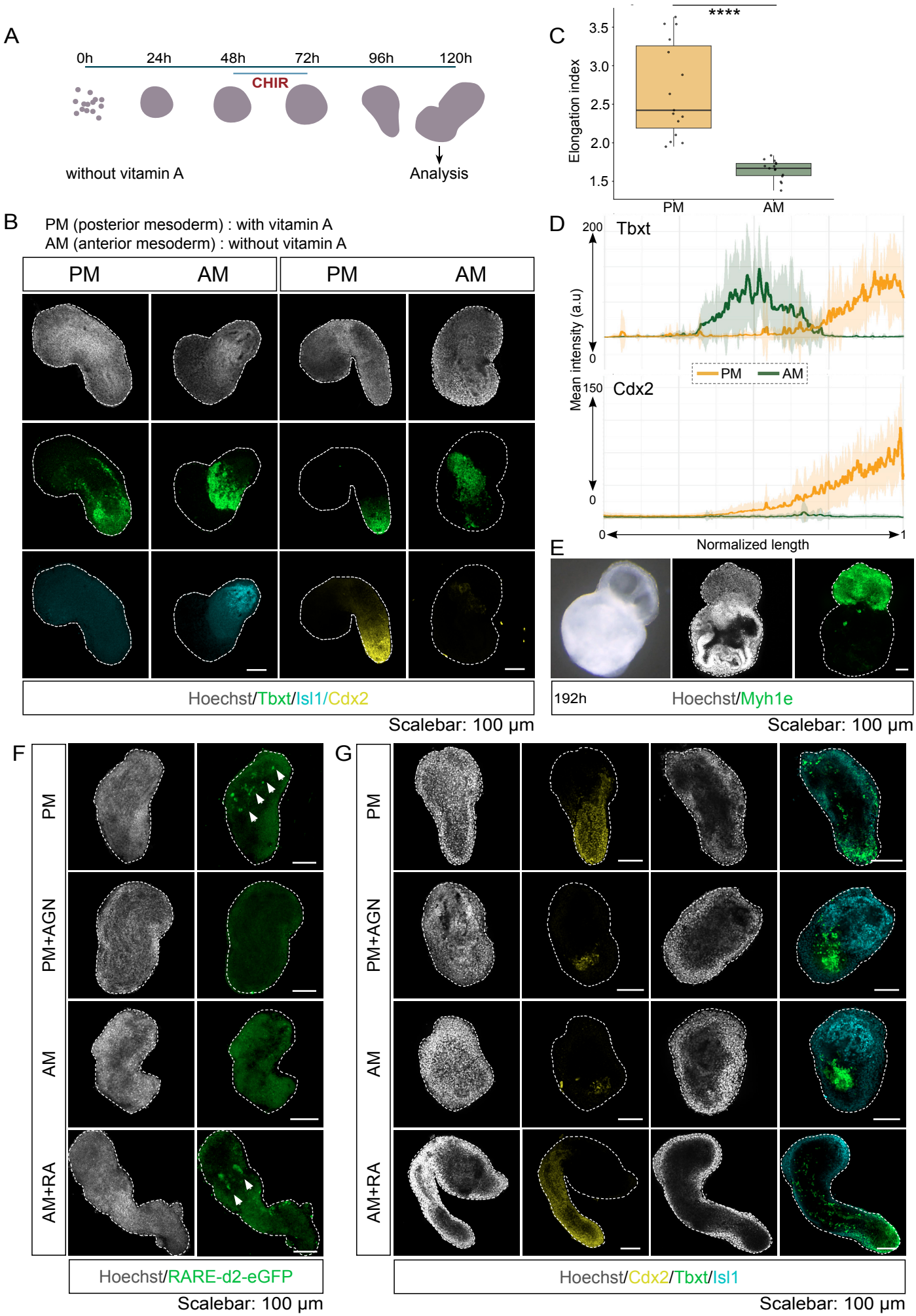
A
0h
24h
48h
72h
96h
120h
CHIR
without vitamin A
Analysis
B
PM (posterior mesoderm) : with vitamin A
AM (anterior mesoderm) : without vitamin A
PM
AM
PM
AM
Hoechst/Tbxt/Isl1/Cdx2
Scalebar: 100 µm
C
****
Elongation index
3.5
3.0
2.5
2.0
1.5
PM
AM
D
Tbxt
Cdx2
Mean intensity (a.u)
200
0
150
0
PM
AM
0
1
Normalized length
E
192h
Hoechst/Myh1e
Scalebar: 100 µm
F
PM
PM+AGN
AM
AM+RA
Hoechst/RARE-d2-eGFP
Scalebar: 100 µm
G
PM
PM+AGN
AM
AM+RA
Hoechst/Cdx2/Tbxt/Isl1
Scalebar: 100 µm

**Figure 1. Removal of vitamin A or inhibition of retinoic acid signaling induces anterior mesoderm in gastruloids**

(A) Schematic of the gastruloid generation protocol. To preclude retinoic acid (RA) signaling, B27 supplement without vitamin A, the biosynthetic precursor of RA, was used. CHIR - CHIR99021, a small molecule Wnt signal agonist.

(B) Confocal images of gastruloids immunostained for the indicated markers. Tbxt (T/Brachyury); N = 6 experimental replicates, n = 50 PM gastruloids, and n = 66 AM gastruloids, posterior marker - Cdx2 (N = 3, n = 24 PM, and 24 AM gastruloids), anterior mesoderm marker - Isl1 (N = 3, n = 22 PM, and 28 AM gastruloids).

(C) Comparison of cell elongation index between posterior mesoderm (PM) and anterior mesoderm (AM) gastruloids. Box plots show the median (central line), interquartile range (box), and individual data points. Paired t-test, n = 15 PM and 15 AM; ****$p < 0.0001$.

(D) Line-scan quantification of Tbxt and Cdx2 expression along the long-axis of gastruloids from the experiment shown in (B). Intensity profiles along the length of gastruloids were obtained using the Fiji line segment tool, and gastruloid lengths were normalized between 0 and 1. The solid line traces the mean intensity (n=17 PM and 15 AM gastruloids), and the shaded region denotes the standard deviation.

(E) Brightfield image and confocal images of immunostained RA-precluded gastruloids induced with a cardiogenic cocktail from 120 to 192 hours. Analysis at 192h revealed the formation of cardiac organoids expressing Myh14. Bright-field imaging reveals chambered organization in some of the cardiac organoids. (N = 4; n =15).

(F) Confocal images of immunostained gastruloids. (N = 4, n = 23 PM, n = 25 PM + AGN, n = 23 AM, n = 26 AM + RA). AGN193109 (AGN) is an inverse agonist of retinoic acid receptors (RARs). Exogenous RA was added to AM gastruloids.

(G) Confocal images of immunostained gastruloids. Isl1/Tbxt (N = 3, n = 20 AM, 14 AM + RA, 14 PM, 18 PM + AGN), Cdx2 (N = 3, n = 19 AM, 22 AM + RA, 23 PM, 17 PM + AGN).

*Scale bar: 100 µm. All confocal images are represented as maximum intensity projections of z-stacks.*

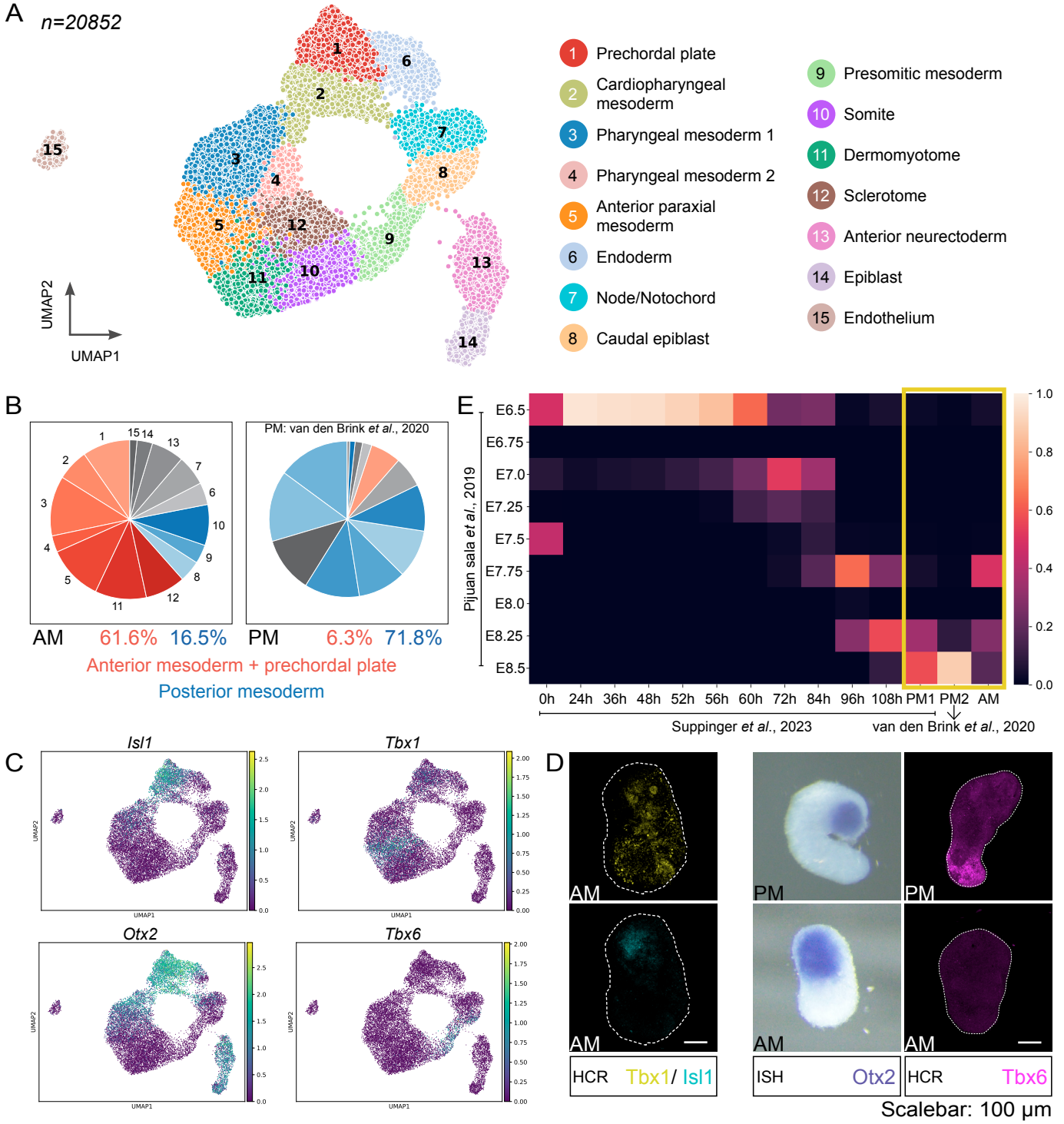
A
n=20852
UMAP2
UMAP1
1 Prechordal plate
2 Cardiopharyngeal mesoderm
3 Pharyngeal mesoderm 1
4 Pharyngeal mesoderm 2
5 Anterior paraxial mesoderm
6 Endoderm
7 Node/Notochord
8 Caudal epiblast
9 Presomitic mesoderm
10 Somite
11 Dermomyotome
12 Sclerotome
13 Anterior neurectoderm
14 Epiblast
15 Endothelium
B
PM: van den Brink et al., 2020
AM 61.6% 16.5%
PM 6.3% 71.8%
Anterior mesoderm + prechordal plate
Posterior mesoderm
E
Pijuan sala et al., 2019
E6.5
E6.75
E7.0
E7.25
E7.5
E7.75
E8.0
E8.25
E8.5
0h 24h 36h 48h 52h 56h 60h 72h 84h 96h 108h PM1 PM2 AM
Suppinger et al., 2023
van den Brink et al., 2020
C
Isl1
Tbx1
Otx2
Tbx6
D
AM
PM
HCR Tbx1/ Isl1
ISH Otx2
HCR Tbx6
Scalebar: 100 µm

**Figure 2. Single-cell transcriptomics reveal the anterior identity of RA signalling-precluded gastruloids**

(A) UMAP plot of sc-RNA-seq data of 120h AM-gastruloids. *n=20852* cells obtained from 192 gastruloids pooled from 3 independent replicates.

(B) Pie-chart comparing the relative proportions of anterior mesoderm (red) and posterior (blue) mesoderm-related clusters in AM gastruloids with those of PM gastruloids (van den Brink et al, 2020). Although it predominantly generates endoderm, we have included the prechordal plate cluster in the anterior mesoderm compartment, as it also gives rise to the prechordal mesoderm.

(C) Gene interrogation plots for select marker genes: *Tbx1* and *Isl1* (cardiopharyngeal and pharyngeal mesoderm), *Otx2* (broad anterior), and *Tbx6* (posterior mesoderm).

(D) Left panel: Confocal images of PM and AM gastruloids assayed using hybridization chain reaction (HCR). The broad domain of *Tbx1* expression and the spatially restricted *Isl1* expression (N = 3 experimental replicates, n = 20 gastruloids AM) are consistent with the single-cell sequencing data. Center panel: Brightfield images of gastruloids stained for *Otx2* mRNA by whole-mount in situ RNA hybridization (N = 3, n = 28 PM and 35 AM). Right panel: *Tbx6* HCR (N = 3, n = 11 PM and 11 AM). *Scale bar: 100 µm. All confocal images are represented as maximum intensity projections of z-stacks.*

(E) Staging of AM gastruloids. An SCMAP projection of sc-seq data of AM gastruloids onto the mouse embryo single-cell gastrulation atlas to stage the gastruloids with respect to the embryonic age of mouse embryos. PM gastruloid datasets, 1 and 2, from the indicated references are also projected for comparison.

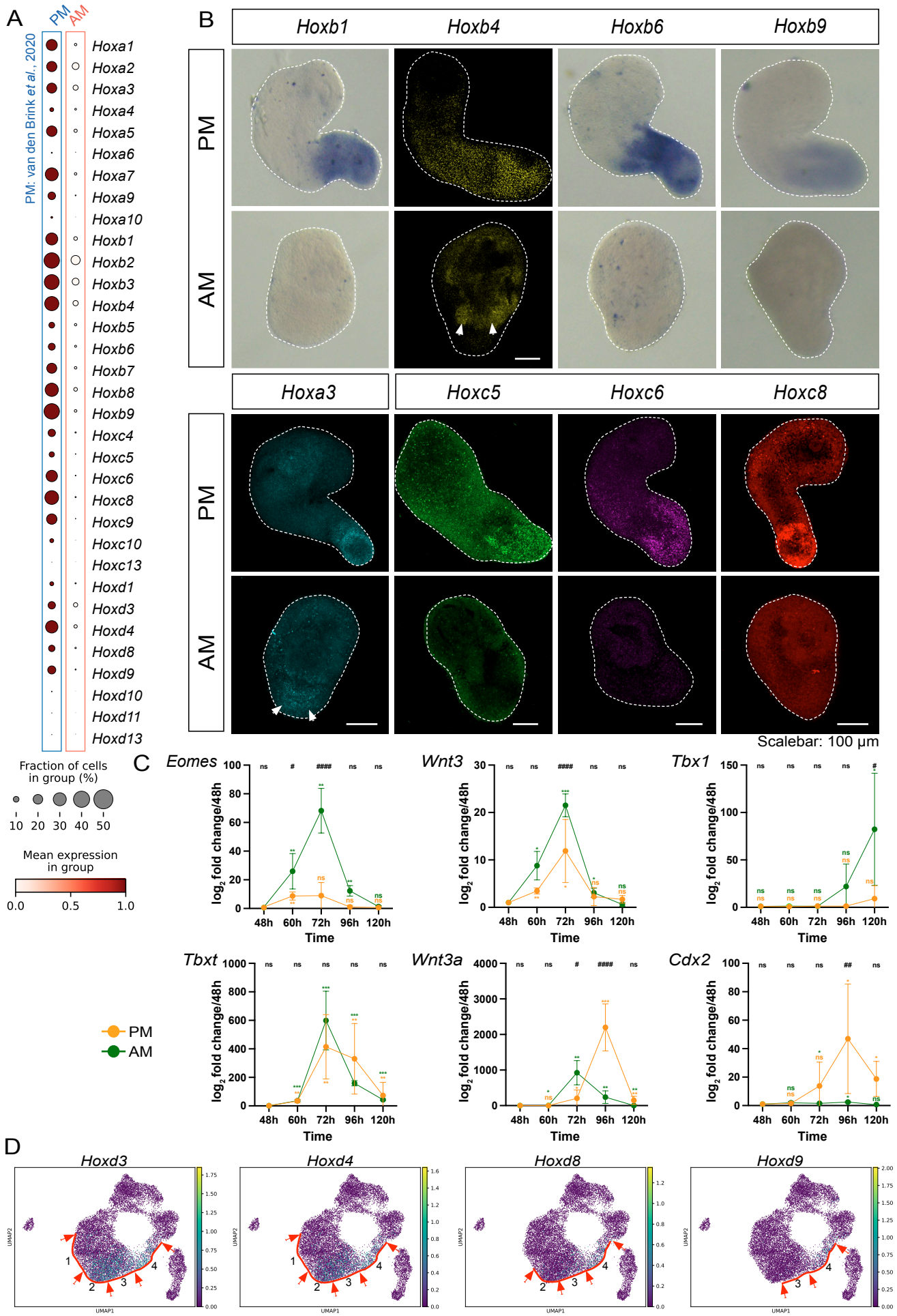
A
PM
AM
PM: van den Brink et al., 2020
Hoxa1
Hoxa2
Hoxa3
Hoxa4
Hoxa5
Hoxa6
Hoxa7
Hoxa9
Hoxa10
Hoxb1
Hoxb2
Hoxb3
Hoxb4
Hoxb5
Hoxb6
Hoxb7
Hoxb8
Hoxb9
Hoxc4
Hoxc5
Hoxc6
Hoxc8
Hoxc9
Hoxc10
Hoxc13
Hoxd1
Hoxd3
Hoxd4
Hoxd8
Hoxd9
Hoxd10
Hoxd11
Hoxd13
Fraction of cells in group (%)
10 20 30 40 50
Mean expression in group
0.0 0.5 1.0
B
Hoxb1
Hoxb4
Hoxb6
Hoxb9
PM
AM
Hoxa3
Hoxc5
Hoxc6
Hoxc8
Scalebar: 100 µm
C
Eomes
Wnt3
Tbx1
Tbxt
Wnt3a
Cdx2
log2 fold change/48h
Time
48h 60h 72h 96h 120h
PM
AM
D
Hoxd3
Hoxd4
Hoxd8
Hoxd9
UMAP1
UMAP2
1. Anterior paraxial mesoderm ; 2. Dermamytome/Sclerotome ; 3. Somite ; 4. Presomitic mesoderm

**Figure 3. Transition to posterior program is repressed in AM gastruloids**

(A) Dotplots of *Hox* gene expression in the merged PM (van den Brink et al., 2020) and AM single-cell datasets. Merging the datasets involves batch correction, which allows comparison.

(B) Confocal and brightfield micrographs of gastruloids assayed by HCR and whole-mount chromogenic in situ hybridization (ISH), respectively. *Hoxb1* (N = 3 experimental replicates, n = 21 PM and 22 AM gastruloids), *Hoxb4* (N = 3, n = 10 PM and 9 AM), *Hoxb6* (N = 3, n = 21 PM and 25 AM), *Hoxb9* (N = 3, n = 25 PM and 19 AM), *Hoxa3* (N = 3, n = 15 PM and 16 AM), *Hoxc5* (N = 3, n = 17 PM and 17 AM), *Hoxc6* (N = 3, n = 11 PM and 11 AM), and *Hoxc8* (N = 3, n = 21 PM and 22 AM). *Scale bar: 100 µm. All confocal images are represented as maximum intensity projections of z-stacks.*

(C) Comparison of gene expression trends across timepoints in PM and AM gastruloids. Data is represented as $\log_2$ fold change relative to the 48h timepoint. Data represent mean ± SD of three biological replicates. Each replicate contained multiple gastruloids per time point (48h and 60h, n = 96 gastruloids; 72 and 96h, n = 72; 120h, n = 48). Post-hoc Sidak multiple comparisons, following a two-way ordinary ANOVA (see Methods), were performed between PM and AM at each time point. Statistical significance is indicated by hashtags (#) at the top of each graph. A two-tailed t-test was performed to compare changes over time within each condition. Significance is indicated by asterisks (*) above or below the error bars. Significance: *,# $P \leq 0.05$; **,## $P \leq 0.01$; ***,### $P \leq 0.001$; ****,#### $P \leq 0.0001$, ns = non-significant ($P > 0.05$).

(D) Gene interrogation plots of the *Hoxd* genes showcase the spatial collinearity of *Hox* gene expression in AM gastruloids. *Hoxd3*, *Hoxd4* are enriched in differentiated somitic clusters, whereas *Hoxd8*, *Hoxd9* show restricted expression in undifferentiated somites and presomitic mesoderm. Red arrows indicate cluster boundaries. The red lines trace expression boundaries.

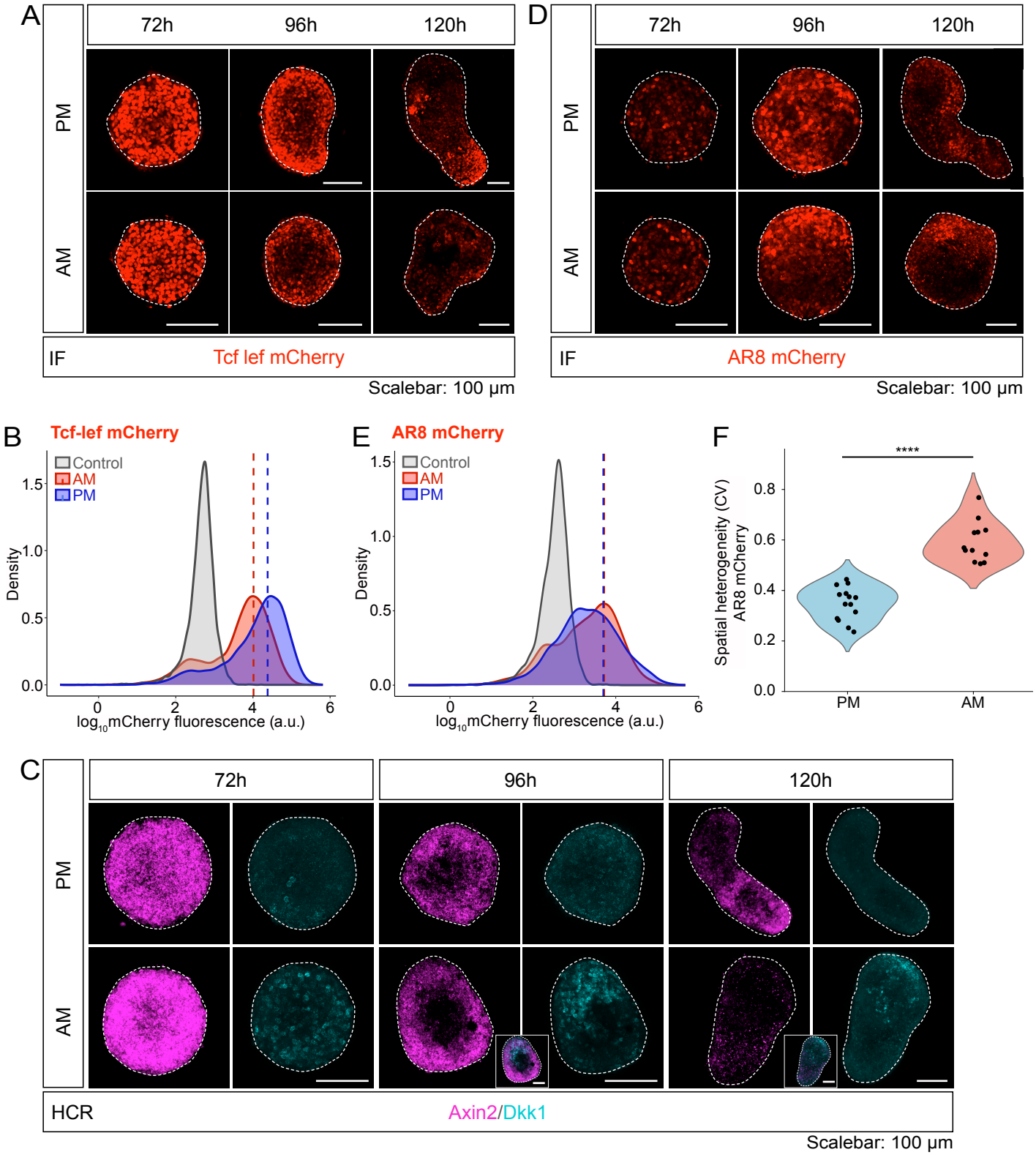
A
72h
96h
120h
PM
AM
IF
Tcf lef mCherry
Scalebar: 100 µm
D
72h
96h
120h
PM
AM
IF
AR8 mCherry
Scalebar: 100 µm
B
Tcf-lef mCherry
Control
AM
PM
Density
log10mCherry fluorescence (a.u.)
E
AR8 mCherry
Control
AM
PM
Density
log10mCherry fluorescence (a.u.)
F
****
Spatial heterogeneity (CV)
AR8 mCherry
PM
AM
C
72h
96h
120h
PM
AM
HCR
Axin2/Dkk1
Scalebar: 100 µm

**Figure 4. Absence of RA signaling attenuates Wnt signaling and restricts the Nodal signaling domain**

(A) Confocal images of *Tcf-Lef:mCherry* reporter gastruloids immunostained with anti-mCherry antibody. (N = 3 experimental replicates, 72h (n = 20 PM and 19 AM gastruloids); 96h (n= 21 PM and 22 AM); 120h (n= 24 PM and 24 AM).

(B) Flow cytometric analysis of 120h *Tcf-Lef:mCherry* reporter gastruloids**.** The positive threshold was set at 95% of cells from the negative control (unlabelled *E14Tg2a* mESCs). Dotted lines mark the median mCherry fluorescence of the samples. Similar results were obtained from 3 independent experiments; each sample is a pool of 48 individual gastruloids.

(C) Confocal images of gastruloids assayed by HCR for *Axin2* (Wnt signalling target) and *Dkk1* (Wnt inhibitor). 72h (N = 3, n = 12 PM and 14 AM gastruloids); 120h (N = 4, n = 19 PM and 16 AM). Insets show the merge of both channels.

(D) Confocal images of gastruloids immunostained for *AR8:mCherry* reporter expression 72h (N = 3, n = 17 PM, and 19 AM); 96h (N = 3, n = 19 PM, and 21 AM); 120h (N = 3, n = 27 PM, and 22 AM).

*Scale bar: 100 µm. All confocal images are represented as maximum intensity projections of z-stacks.*

(E) Flow analysis of 120h *AR8:mCherry* reporter gastruloids. Dotted lines indicate the median fluorescence intensity. (N = 3, 48 gastruloids pooled per replicate).

(F) Quantification of spatial heterogeneity (coefficient of variation, CV) of *AR8:mCherry* expression in anterior mesoderm (AM) and posterior mesoderm (PM) gastruloids. Each point represents one gastruloid; violins indicate data distribution. Statistical significance was assessed using a two-sided Mann–Whitney U test ($U = 168$, $p = 1.74 \times 10^{-5}$).

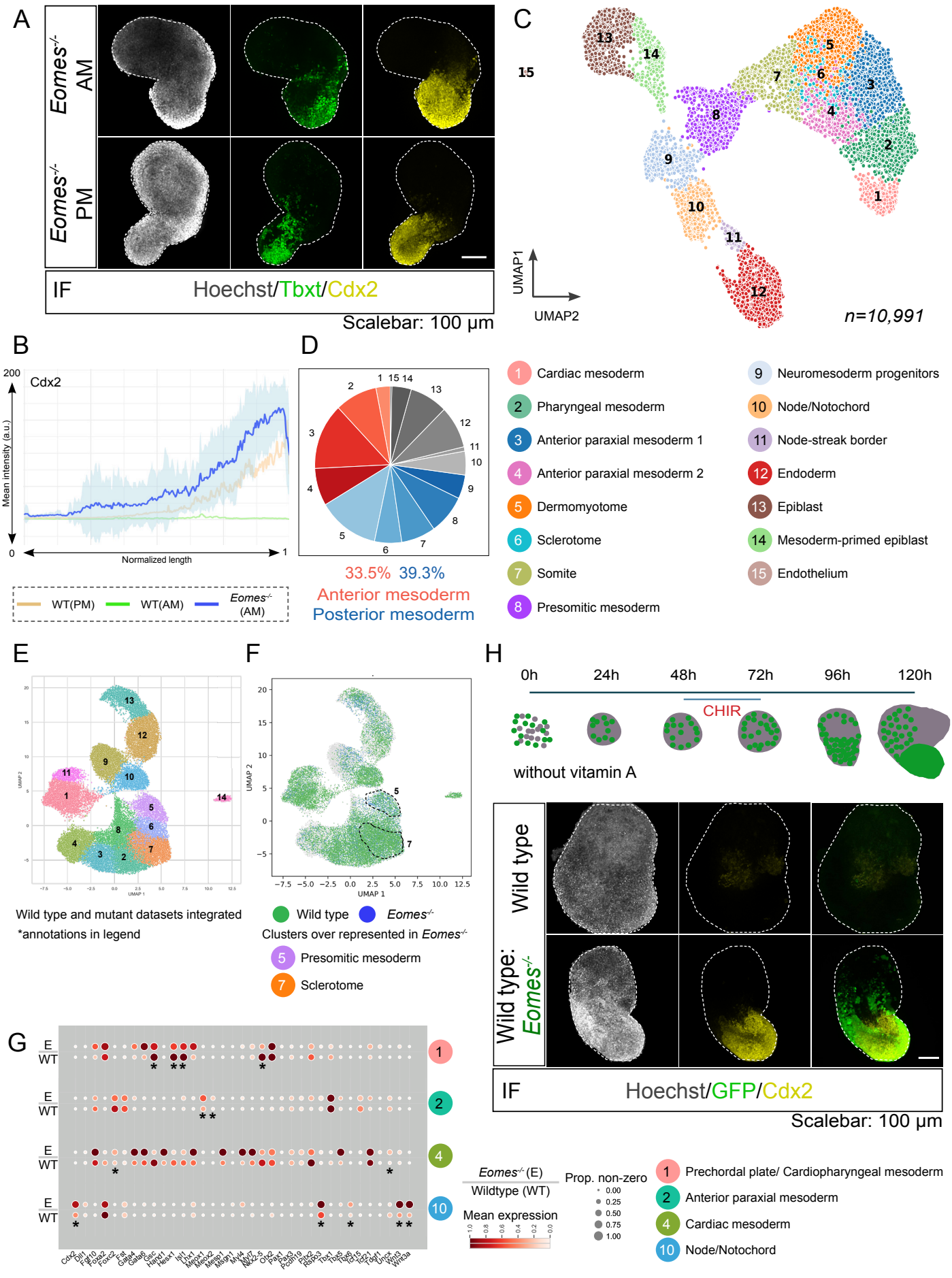
A
Eomes-/- AM
Eomes-/- PM
IF
Hoechst/Tbxt/Cdx2
Scalebar: 100 µm
C
UMAP1
UMAP2
n=10,991
B
Cdx2
Mean intensity (a.u.)
Normalized length
WT(PM)
WT(AM)
Eomes-/- (AM)
D
33.5% 39.3%
Anterior mesoderm
Posterior mesoderm
1 Cardiac mesoderm
2 Pharyngeal mesoderm
3 Anterior paraxial mesoderm 1
4 Anterior paraxial mesoderm 2
5 Dermomyotome
6 Sclerotome
7 Somite
8 Presomitic mesoderm
9 Neuromesoderm progenitors
10 Node/Notochord
11 Node-streak border
12 Endoderm
13 Epiblast
14 Mesoderm-primed epiblast
15 Endothelium
E
Wild type and mutant datasets integrated
*annotations in legend
F
Wild type
Eomes-/-
Clusters over represented in Eomes-/-
5 Presomitic mesoderm
7 Sclerotome
H
0h
24h
48h
72h
96h
120h
CHIR
without vitamin A
Wild type
Wild type: Eomes-/-
IF
Hoechst/GFP/Cdx2
Scalebar: 100 µm
G
E
WT
Eomes-/- (E)
Wildtype (WT)
Mean expression
Prop. non-zero
1 Prechordal plate/ Cardiopharyngeal mesoderm
2 Anterior paraxial mesoderm
4 Cardiac mesoderm
10 Node/Notochord

**Figure 5. Posterior fate is induced in *Eomes* mutants despite the absence of RA signaling**

(A) Confocal images of gastruloids immunostained for Tbxt (T/Brachyury) and posterior marker Cdx2. *Eomes*$^{-/-}$ (N = 5 experiments, n = 20 PM and 40 AM gastruloids).

(B) Line-scan quantification of Cdx2 expression along the long-axis of *Eomes*$^{-/-}$ AM gastruloids (n = 16). Intensity profiles along the length of gastruloids were obtained using the Fiji line segment tool and gastruloid lengths of gastruloids were obtained using the Fiji line segment tool and gastruloids lengths were normalized between 0 and 1. The solid line indicates the mean intensity, and the shaded region denotes the standard deviation. The lighter orange and green mean intensity lines represent line-scan quantification of Cdx2 expression in wild type PM and AM gastruloids from Figure 1, shown here for comparison.

(C) UMAP plot of sc-RNA-seq data of 120h *Eomes*$^{-/-}$ AM gastruloids. n = *10,991* cells obtained from 144 gastruloids pooled from 2 independent replicates.

(D) Pie-chart comparing the relative proportions of anterior (red) and posterior (blue) mesoderm-related clusters in *Eomes*$^{-/-}$ AM gastruloids.

(E) UMAP plot of the integrated dataset of wild type, *Eomes*$^{-/-,}$ and *Tbxt*$^{-/-}$ AM gastruloids. The 14 clusters obtained were annotated based on the expression of marker genes. Annotations: 1-Prechordal plate & Cardiopharyngeal mesoderm, 2-Anterior paraxial mesoderm, 3-Pharyngeal mesoderm, 4-Cardiac mesoderm, 5-Presomitic mesoderm, 6-Somites, 7-Sclerotome, 8-Dermomyotome, 9-Neuromesoderm progenitors & Spinal cord, 10-Node/Notochord, 11-Endoderm, 12-Caudal epiblast, 13-Epiblast, 14-Endothelium.

(F) UMAP showing co-embedding of wild type (green) and *Eomes*$^{-/-}$ (blue) AM gastruloid single-cell datasets. *Tbxt*$^{-/-}$ dataset is masked (grey). The clusters with a higher representation from the *Eomes*$^{-/-}$ dataset are highlighted with a dotted line.

(G) The dot plot illustrates the expression of select marker genes in both wild type and *Eomes*$^{-/-}$ samples derived from the integrated single-cell RNA sequencing datasets. The color of the dots (red) signifies the average scaled gene expression, whereas the size of the dots indicates the percentage of cells expressing the gene within each cluster. Notable differences in expression are indicated by asterisks (*). Genes associated with the anterior regions, such as *Gsc, Hesx1, Isl1,* and *Nkx2-5*, exhibited reduced expression in *Eomes*$^{-/-}$ compared to the wild type, particularly within the prechordal plate/CPM cluster. Conversely, genes associated with the posterior regions showed increased expression in *Eomes*$^{-/-}$, *Foxc2* and *Uncx,* in the cardiac mesoderm, *Meox1* and *Meox2* in the anterior paraxial mesoderm, and *Cdx2, Rspo3, Tbx6*, and *Wnt3a* in the node/notochord cluster.

(H) Confocal images of chimeric AM gastruloids, wild type:*Eomes*$^{-/-}$*-GFP* in 50:50 ratio, immunostained for GFP and Cdx2. Wild type (N = 3, n = 31) and *Eomes*$^{-/-}$*-GFP* (N = 3, n = 30).

*Scale bar: 100 µm. All confocal images are represented as maximum intensity projections of z-stacks.*

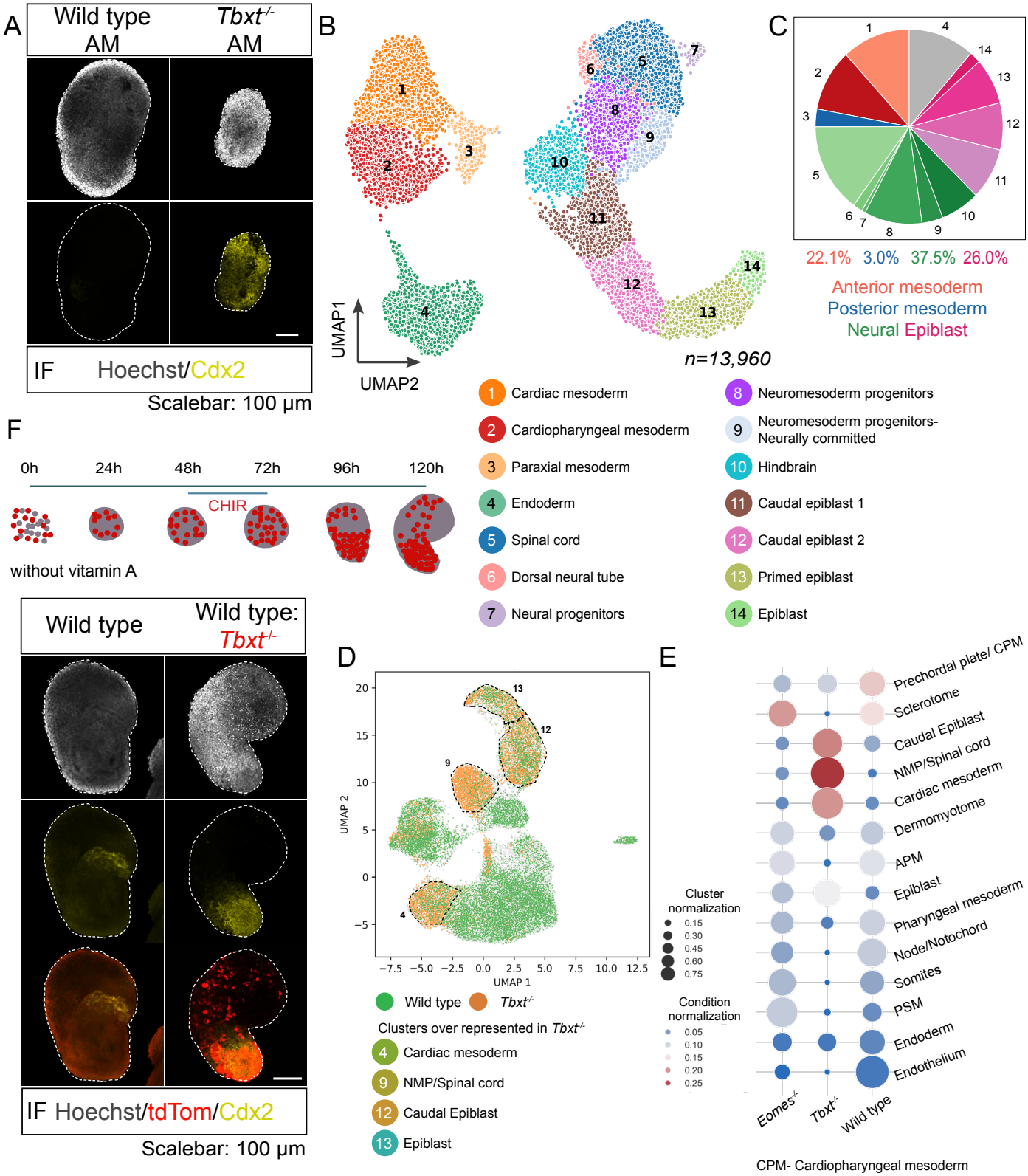
A
Wild type AM
Tbxt-/- AM
IF Hoechst/Cdx2
Scalebar: 100 µm
B
UMAP1
UMAP2
n=13,960
C
22.1% 3.0% 37.5% 26.0%
Anterior mesoderm
Posterior mesoderm
Neural Epiblast
1 Cardiac mesoderm
2 Cardiopharyngeal mesoderm
3 Paraxial mesoderm
4 Endoderm
5 Spinal cord
6 Dorsal neural tube
7 Neural progenitors
8 Neuromesoderm progenitors
9 Neuromesoderm progenitors- Neurally committed
10 Hindbrain
11 Caudal epiblast 1
12 Caudal epiblast 2
13 Primed epiblast
14 Epiblast
F
0h 24h 48h 72h 96h 120h
CHIR
without vitamin A
Wild type
Wild type: Tbxt-/-
IF Hoechst/tdTom/Cdx2
Scalebar: 100 µm
D
UMAP 1
UMAP 2
Wild type
Tbxt-/-
Clusters over represented in Tbxt-/-
4 Cardiac mesoderm
9 NMP/Spinal cord
12 Caudal Epiblast
13 Epiblast
E
Cluster normalization
0.15
0.30
0.45
0.60
0.75
Condition normalization
0.05
0.10
0.15
0.20
0.25
Prechordal plate/ CPM
Sclerotome
Caudal Epiblast
NMP/Spinal cord
Cardiac mesoderm
Dermomyotome
APM
Epiblast
Pharyngeal mesoderm
Node/Notochord
Somites
PSM
Endoderm
Endothelium
Eomes-/-
Tbxt-/-
Wild type
CPM- Cardiopharyngeal mesoderm
APM- Anterior Paraxial mesoderm
PSM- Presomitic mesoderm
NMP- Neuromesoderm progenitors

**Figure 6. Loss of function of *Tbxt* activates posterior neural fate despite the absence of RA signaling**

(A) Confocal images of gastruloids immunostained for the posterior marker Cdx2. Wild type (N = 3 experimental replicates, n = 16 AM gastruloids), *Tbxt*$^{-/-}$ (N = 3, n = 15 AM gastruloids).

(B) UMAP plot of sc-RNA-seq data of 120h gastruloids *Tbxt*$^{-/-}$ AM gastruloids. *n=13,960* cells obtained from 192 gastruloids pooled from 2 independent replicates.

(C) Pie-chart comparing the relative proportions of anterior (red) and posterior (blue) mesoderm-related, neural (green) and epiblast (pink) clusters in *Tbxt*$^{-/-}$ AM gastruloids.

(D) UMAP showing co-embedding of wild type (green) and *Tbxt*$^{-/-}$ (orange) AM gastruloid datasets. *Eomes*$^{-/-}$ dataset is masked (grey). The clusters with a higher representation from the *Tbxt*$^{-/-}$ dataset are highlighted with a dotted line.

(E) A clustermap comparing the proportion of cells in different clusters within (dot size) and across (dot colour) wild type, *Eomes*$^{-/-}$ and *Tbxt*$^{-/-}$ datasets. It was generated after the integration of the datasets.

(F) Confocal images of chimeric AM gastruloids, wild type:*Tbxt*$^{-/-}$*-tdTomato* in 50:50 ratio, immunostained for tdTomato and Cdx2. wild type (N = 3, n = 13) and *Tbxt*$^{-/-}$*-tdTomato* (N = 3, n = 28).

*Scale bar: 100 µm. All confocal images are represented as maximum intensity projections of z-stacks.*

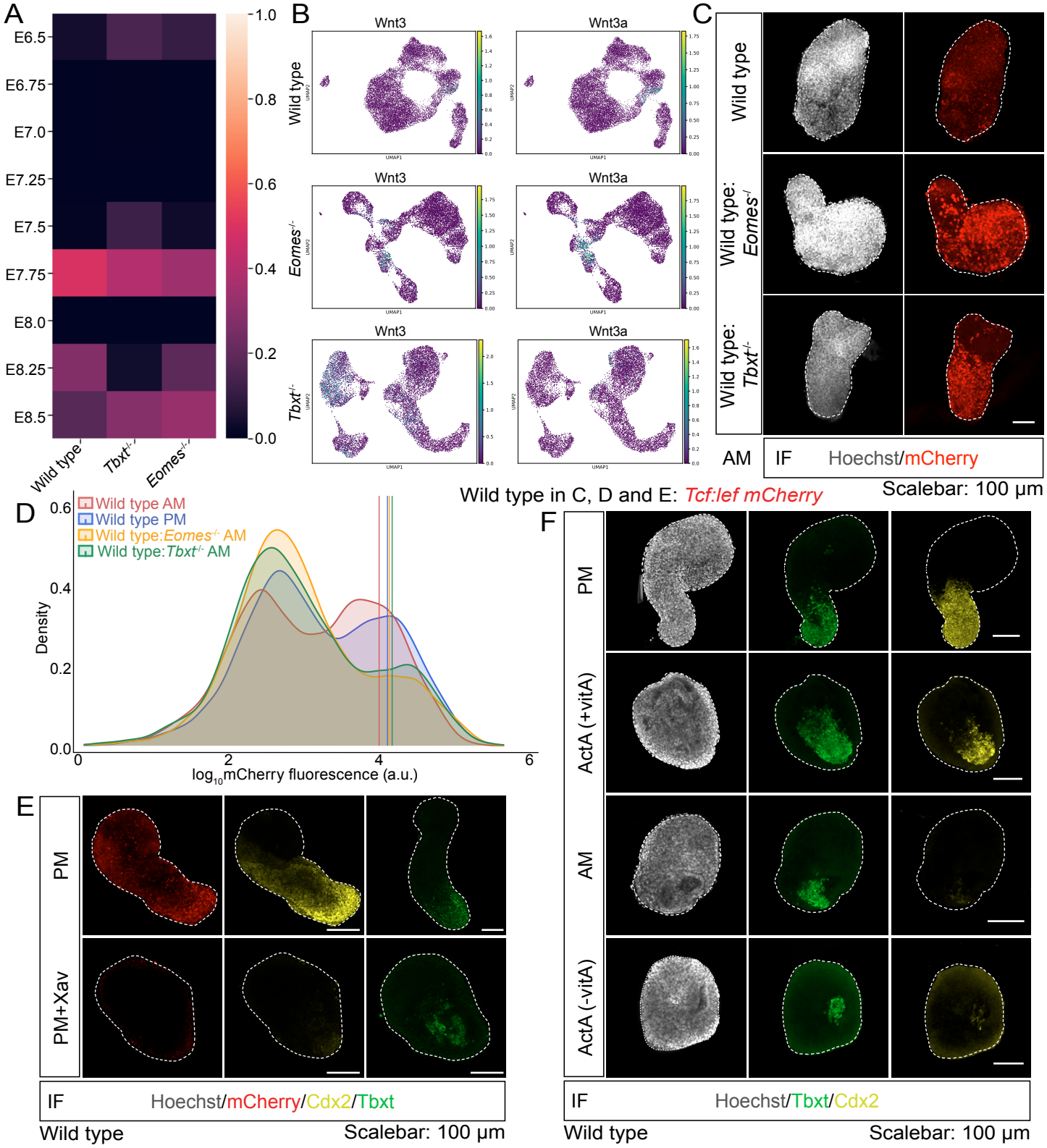
A
E6.5
E6.75
E7.0
E7.25
E7.5
E7.75
E8.0
E8.25
E8.5
Wild type
Tbxt-/-
Eomes-/-
1.0
0.8
0.6
0.4
0.2
0.0
B
Wnt3
Wnt3a
Wild type
Eomes-/-
Tbxt-/-
C
Wild type
Wild type: Eomes-/-
Wild type: Tbxt-/-
AM
IF Hoechst/mCherry
Scalebar: 100 µm
Wild type in C, D and E: Tcf:lef mCherry
D
Wild type AM
Wild type PM
Wild type:Eomes-/- AM
Wild type:Tbxt-/- AM
Density
log10mCherry fluorescence (a.u.)
E
PM
PM+Xav
IF Hoechst/mCherry/Cdx2/Tbxt
Wild type
Scalebar: 100 µm
F
PM
ActA (+vitA)
AM
ActA (-vitA)
IF Hoechst/Tbxt/Cdx2
Wild type
Scalebar: 100 µm

**Figure 7. *Eomes* and *Tbxt* suppress the Wnt-Cdx2 module in the context of anterior mesoderm specification**

(A) SCMAP projection of *Eomes*$^{-/-}$, *Tbxt*$^{-/-}$ and wild type AM gastruloid single cell sequencing data onto the mouse gastrulation atlas to assess the developmental age of the mutant gastruloids.

(B) Gene interrogation plots of *Wnt3* and *Wnt3a* in wild type, *Eomes*$^{-/-}$, and *Tbxt*$^{-/-}$ single-cell UMAPs.

(C) Confocal images showing mCherry expression in wild type, *Eomes*$^{-/-}$, and *Tbxt*$^{-/-}$ chimeric AM gastruloids. *Tcf-lef:mCherry* reporter was used as the wild type. Chimeric gastruloids generated by mixing wild type and mutant cells in a 50:50 ratio during plating (N = 3 experimental replicates, n = 21 wild type; 40 wild type:*Eomes*$^{-/-}$; 27 wild type:*Tbxt*$^{-/-}$ gastruloids).

(D) Flow-cytometric quantification of Wnt reporter activity in wild type (*Tcf-lef:mCherry* reporter) and chimeric AM gastruloids. Median mCherry fluorescence intensity of the *Tcf-Lef:mCherry* reporter was measured in wild type gastruloids under AM and PM conditions, as well as in chimeric AM gastruloids containing wild type and *Eomes*$^{-/-}$ or *Tbxt*$^{-/-}$ cells in a 50:50 ratio. Median intensities were as follows: wild type (AM): 3.983640; wild type (PM): 4.094799; wild type:Eomes$^{-/-}$ (AM): 4.119460; wild type:*Tbxt*$^{-/-}$ (AM): 4.157401.

(E) Confocal microscopy images of indicated markers in PM and PM induced with Xav939 (Wnt inhibitor) from 72 to 120h in *Tcf-Lef:mCherry* reporter gastruloids. mCherry/Cdx2 (N = 3, n = 17 PM and 14 PM+Xav), Tbxt (N = 3, n = 19 PM and 14 PM+Xav).

(F) Confocal imaging of indicated markers upon Activin-A (ActA) substitution for CHIR. (N = 5; n = 31 PM, 37 AM, 27 PM (+ActA), and 37 AM (+ActA)).

*Scale bar: 100 µm. All confocal images are represented as maximum intensity projections of z-stacks.*

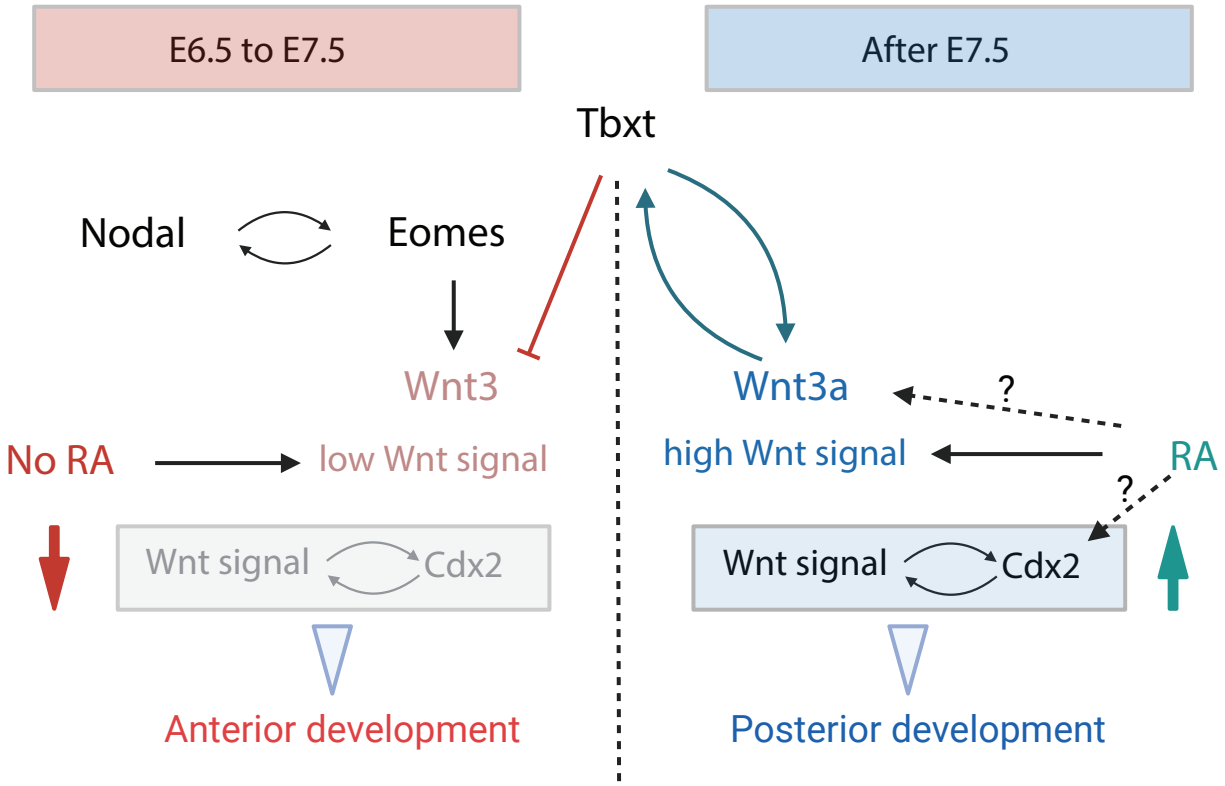
E6.5 to E7.5
After E7.5
Tbxt
Nodal
Eomes
Wnt3
Wnt3a
?
No RA
low Wnt signal
high Wnt signal
RA
?
Wnt signal
Cdx2
Wnt signal
Cdx2
Anterior development
Posterior development

**Figure 8. RA signalling regulates the orderly anterior to posterior transition of the mesoderm developmental program**

Model summarizing the role of RA signaling in the mesoderm gene regulatory network governing the orderly developmental progression from anterior to posterior program. Between E6.5–E7.5, in the absence of RA, activation of the posterior program is prevented by maintaining Wnt signalling at a lower level. During this period, *Eomes* and *Tbxt* independently restrict premature posterior specification by downregulating Wnt activity through Wnt3a and Wnt3, respectively, thereby preventing activation of the Wnt–Cdx2 module and supporting anterior development. After E7.5, when RA signalling becomes active, a higher threshold of Wnt signalling is achieved by stabilizing the Tbxt–Wnt3a–Cdx2 module, which promotes posterior specification. Dashed arrows denote predicted RA-dependent regulation of Wnt3a and Cdx2.